Impact behavior of auxetic cementitious cellular composites (ACCCs) architected through additive manufacturing (AM) assisted casting
Experiment and modelling

Xie, Jinbao; Xu, Yading; Meng, Zhaozheng; Liang, Minfei; Zhou, Yubao; Šavija, Branko

DOI
10.1016/j.conbuildmat.2025.140692

Publication date
2025

Document Version
Final published version

Published in
Construction and Building Materials

Construction and Building Materials 471 (2025) 140692

Contents lists available at ScienceDirect

Construction and Building Materials

journal homepage: www.elsevier.com/locate/conbuildmat

Impact behavior of auxetic cementitious cellular composites (ACCCs) architected through additive manufacturing (AM) assisted casting: Experiment and modelling

Jinbao Xie *, Yading Xu, Zhaozheng Meng, Minfei Liang, Yubao Zhou, Branko Šavija

Faculty of Civil Engineering and Geosciences, Delft University of Technology, Delft 2628CN, the Netherlands

ARTICLE INFO

Keywords:
Auxetic cementitious cellular composites
Additive manufacturing
Impact loading
Energy absorption
Impact model
Strain rate effect

ABSTRACT

Auxetic cementitious cellular composites (ACCCs) possess advantageous mechanical properties in static tests, such as high fracture resistance and efficient energy dissipation. However, little attention has been given to understanding the impact resistance of ACCCs. In this study, two typical elliptical-shaped ACCC specimens, P25 and P50, were designed with major axis lengths increased by 25 % and 50 %, respectively, compared to the reference P0 with circular holes. The specimens were architected through additive manufacturing (AM) assisted casting, and subjected to low-velocity impacts from Schmidt hammer with a consistent initial impact energy. Their impact resistance was assessed based on impact responses, including rebound value, absorption energy, localized damage in the impact zone, crack propagation, and peak reaction force during impact. Besides single impact tests, multiple impact tests were conducted until specimens failed. Their impact results were compared with those of the reference (P0). A high-speed camera was further used for Digital Image Correlation (DIC) to analyze strain distribution of the specimens during the brief impact period. Furthermore, a numerical model considering strain rate effects was developed to simulate the impact behavior of ACCCs, demonstrating good agreement with experimental data. On this basis, a parametric analysis was performed to evaluate the effects of impact energy, relative density, specimen size, and RVE size on impact resistance. Both experimental and numerical results indicate that ACCCs demonstrate superior impact resistance compared to the reference (P0). They exhibit mitigated localized damage in the impact zone and increased contact stiffness. Moreover, ACCCs show greater endurance under multiple impacts and higher accumulated energy absorption until failure. This enhanced performance is attributed to auxetic behavior, which draws more material into the impact zone for dispersing energy and reducing localized damage, thereby maintaining overall structural integrity. Specifically, P50 exhibits higher impact resistance than P25 due to the enhanced auxetic behavior resulting from its greater aspect ratio. This creates a greater bending moment to enable more ligaments to dissipate energy through rotation-induced plastic deformation, thereby reducing localized damage. Considering the widespread availability of cementitious materials, this study highlights the potential of ACCCs for lightweight, high-performance protective structural materials for impact mitigation in infrastructure.

1. Introduction

Low-velocity impact events occur in various infrastructure scenarios, such as roofs struck by hailstorms and rockfall, vehicle or vessel collisions with bridge pillars [1], and ships collision with docks in harbors. High-velocity impact events, including debris on runways [2], fragments from blast loads [3], and ballistic or projectile impacts [4], can also cause severe structural damage. As extreme dynamic loadings, impact loadings involve a significant transfer of energy within a short duration and often occur in succession, leading to severe localized damage in the impact zone and further compromising structural integrity. This can cause catastrophic damage and infrastructure collapse, resulting in significant human and economic losses. The risk of civil and military infrastructures—including buildings, bridges, tunnels, roads—being exposed to impact loadings is increasing globally.

Concrete stands out as the most advantageous material for impact

* Corresponding author.
E-mail addresses: J.Xie-1@tudelft.nl (J. Xie), y.xu-5@tudelft.nl (Y. Xu), Z.Meng@tudelft.nl (Z. Meng), M.Liang@tudelft.nl (M. Liang), y.zhou-16@tudelft.nl (Y. Zhou), B.Savija@tudelft.nl (B. Šavija).

https://doi.org/10.1016/j.conbuildmat.2025.140692
Received 13 October 2024; Received in revised form 3 February 2025; Accepted 2 March 2025
Available online 11 March 2025

mitigation in constructing structures, owing to its widespread availability, exceptional performance, and low cost. When adequately reinforced, concrete demonstrates ductile behavior, particularly under tensile loads. For many years, reinforced concrete (RC) structures have been extensively researched for their role in constructing protective infrastructures against impact loading [5–11]. However, due to its quasi-brittle nature, concrete struggles with tensile stress, leading to extensive cracking and brittle failure under impact. This can pose risks to nearby occupants due to high-velocity debris. Incorporating fibers into the brittle cementitious matrix, as observed in materials such as strain-hardening cementitious composites (SHCC), notably boosts tensile performance by enabling large tensile strain. This enhancement assists in resisting crack development and propagation under impact loading, facilitated by fiber bridging. Consequently, this modification shifts the failure mode from brittle to pseudo-plastic, thereby enhancing the structural integrity and safety of the material [12–15]. Nevertheless, high-performance fiber-reinforced cementitious materials still exhibit outward material flow from the impact zone during low-velocity drop-weight impacts [16,17]. This results in reduced material volume and diminished resistance to indentation. In the case of Split-Hopkinson Pressure Bar (SHPB) tests and ballistic penetration under high-velocity impacts, it can even lead to splitting and complete perforation [15,18]. Such localized damage compromises structural integrity, limiting the ability to engage additional material to effectively resist further impacts.

Auxetic materials, characterized by a negative Poisson's ratio, exhibit lateral contraction in the perpendicular direction when subjected to compression [19–22]. The lateral contraction results in a densification of the material at the impact point by pulling material into the impacted zone, consequently improving impact resistance to indentation and shear [4,22]. Moreover, auxetic structures achieve increasing material deformation and crack resistance by pulling the material inward laterally, thereby achieving higher energy absorption. Furthermore, the higher porosity in auxetic structures results in lower mass, leading to increased specific energy absorption. These unique characteristics of auxetic materials make them highly desirable for lightweight impact mitigation, offering superior energy absorption, increased fracture toughness, and enhanced damping capabilities. Therefore, many researchers have focused on investigating auxetic metamaterials and their application in protective engineering and various other fields. Static and impact tests have been carried out to evaluate various auxetic structures made from composite materials [23–26]. Additionally, experiments have been performed to assess the protective performance of lightweight auxetic core sandwich structures [27–31], which consists of auxetic cores positioned between two thin but rigid face panels. These auxetic structures effectively adapt to dynamic loading by progressively drawing the material into the locally loaded zone, thereby enhancing energy absorption and improving impact resistance. Considering the impact behavior of direct local impact on auxetic materials, Gärtner *et al.* [32] explored geometric impacts on elastic impact mitigation within architected auxetic metamaterials by comparing different auxetic structures with a typical non-auxetic honeycomb structure. Among the structures examined, the rotated re-entrant structure exhibited the highest lateral pressure wave speed, indicating significant involvement of surrounding material in dissipating impact energy.

Recently, auxetic cementitious composites have demonstrated favorable mechanical properties in static tests, including high fracture resistance and energy dissipation, due to their unique deformation characteristics. Xu et al. [33] utilized a fiber-reinforced cementitious composite as the foundational material and engineered a cellular structure with regularly spaced elliptical perforations, known as elliptical-shaped auxetic cementitious cellular composites (ACCCs). Undergoing uniaxial compression, the ACCCs exhibited an auxetic behavior characterized by a negative Poisson's ratio. This distinct behavior observed was ascribed to the crack bridging mechanism occurring within the cementitious matrix. Once pre-compressed to a specific displacement, this elliptical-shaped ACCC demonstrated a level of recoverable deformation and a quasi-elastic response when exposed to dynamic cyclic loading [33,34]. On this basis, Xie et al. [35] developed peanut-shaped ACCCs to enhance energy dissipation capability, ductility, and toughness by mitigating stress concentration through the incorporation of peanut-shaped holes. Xu et al. [36] developed a 3D auxetic cementitious-polymeric composite structure (3D-ACPC) comprising a 3D printed polymeric shell and cementitious mortar. This composite exhibits compressive strain-hardening behavior, ensuring a high capacity for energy absorption. Chen et al. [37] fabricated 2D re-entrant, cross-chiral, and buckling-induced auxetic structures using engineered cementitious composites (ECC) and investigated their mechanical response through uniaxial compressive and flexural testing. Xu et al. [38,39] created auxetic cementitious composites by embedding 3D printed polymeric auxetic reinforcement structures within cementitious mortar. These composites demonstrated notable compressive ductility, high recoverable deformability, and superior energy dissipation capability through the reciprocal integration of auxetic structures and cementitious mortar. Nguyen-Van et al. [40] utilized the Primitive minimal surface, one type of the triply periodic minimal surface (TPMS) structure, to reinforce cement-based beams. This configuration demonstrated significant resilience in bearing loads during impact testing. Chen et al. [18] conducted an experimental investigation into the static and dynamic compressive behavior of various structures, including 3D octet, re-entrant honeycomb, and triangular lattice, reinforced with ultra-high performance concrete (UHPC), as well as steel fiber-reinforced UHPC. However, there has been no research on the impact resistance of architected auxetic cementitious materials, leading to a significant gap in our understanding of their mechanical response under impact loading.

This study conducted both experimental and numerical investigations to assess the impact resistance of ACCCs. Two typical ACCCs, labeled as P25 and P50, were manufactured and subjected to impact tests by using a Schmidt hammer. The reaction force for each impact test was recorded. Analysis of the impact test results, which included rebound value, absorption energy, localized damage in the impact zone, crack propagation, and peak reaction force during impact, was performed. A high-speed camera recorded the rapid deformation of ACCCs during impact loading, enabling DIC analysis of strain distribution throughout the process. The impact test results of ACCCs were also compared with those obtained from specimen P0 featuring circular holes. Moreover, a numerical model considering the strain rate effect of the fiber-reinforced cementitious materials was developed to simulate the impact behavior of ACCCs. Afterwards, a parametric analysis was conducted to assess effects of impact energy, relative density, specimen size, and RVE size on impact resistance. Considering the widespread availability of cementitious materials, this study highlights the potential of ACCCs for high-performance protective structural materials for impact mitigation in infrastructure.

2. Experimental tests

2.1. Specimen design and fabrication

The compressive deformation patterns of ACCCs were significantly influenced by their geometric features and constituent materials. The auxetic behavior of ACCCs is induced by the fiber-bridging effect in the constituent fiber-reinforced cementitious material [33]. In our previous study [41], the elliptical-shaped ACCCs with chiral sections (P25 and P50) exhibited a negative Poisson's ratio (i.e., auxetic behavior) during quasi-static compression tests due to the fiber-bridging effect. The numbers in P25 and P50 represent the percentage increase in the length of the major axis compared to P0 with circular holes, corresponding to 25 % and 50 %, respectively. Therefore, specimens P25 and P50 were examined for the impact test. Specimen P0, featuring circular holes,

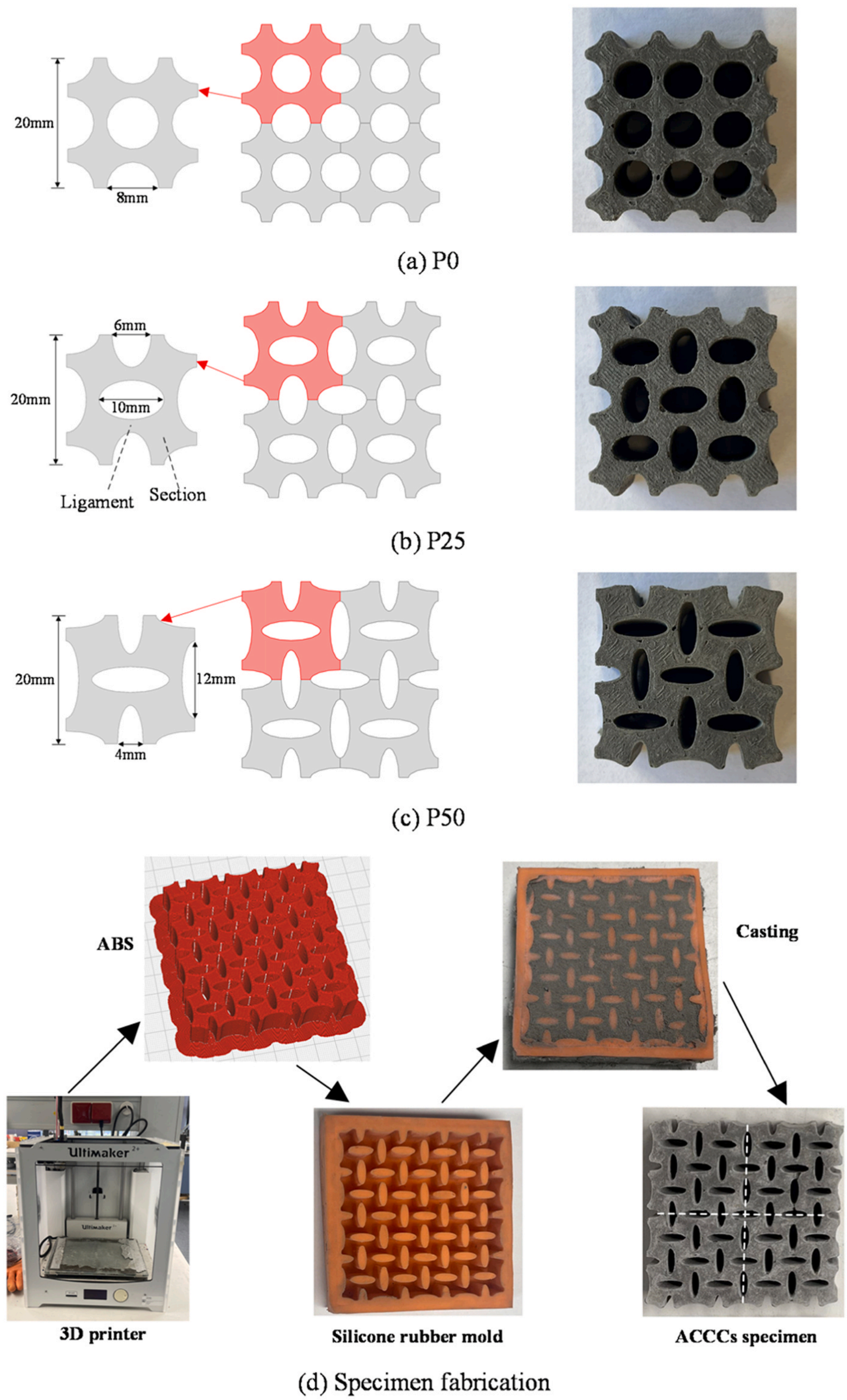

Fig. 1. Specimen design and fabrication.

Table 1
Design parameters of specimens (2 ×2 cell).

Specimen series	Major axis (mm)	Minor axis (mm)	Aspect ratio	One Ellipse area (mm^2)	Specimen side length (mm)	Specimen thickness (mm)	Specimen volume (cm^3)	Relative density
P0	8	8	1.00	50.27	40	20	15.90	49.7 %
P25	10	6	1.67	47.12	40	20	16.93	52.9 %
P50	12	4	3.00	37.70	40	20	19.94	62.3 %

Table 2
Mix ratios of ACCCs (kg/m^3).

Cement	Fly ash	Sand (125 μm to 250 μm)	Water	Superplasticizer (Glenium 51)	VMA	PVA Fiber
453	535	370	450	1.58	0.29	25.6

Table 3
Material properties of PVA fiber.

Diameter (μm)	Length (mm)	Tensile strength (GPa)	Young's modulus (GPa)	Density (g/cm^3)
15	6	1.6	34	1.28

failed to exhibit auxetic behavior in the static compression test, even when fiber-reinforced cementitious materials were used [41]. It was used as a reference for comparative analysis in this study. The design parameters of specimens P0, P25, P50 are shown in Fig. 1 and Table 1. The aspect ratio of the hole within ACCCs was determined as the ratio of its major axis to its minor axis. P50 has a greater aspect ratio than P25, indicating less compressible space.

The quasi-static tests results of the three specimens have been reported in our previous study [41] (see Appendix A). The compressive process of P0 under uniaxial compression was similar to that of conventional fiber-reinforced cementitious materials without auxetic behavior. A single peak formed after the peak load and propagated through the cellular structure. However, P25 and P50 exhibited auxetic behavior under compression and a typical compressive stress–strain response with two peaks was found. This auxetic behavior resulted in a typical compressive stress–strain response characterized by substantial deformation for energy dissipation. Specially, P50 exhibited a greater magnitude of the negative Poisson's ratio than P25 before self-contact within their central elliptical holes during uniaxial compression testing [41].

These specimens were fabricated using the "indirect printing" process and additive manufacturing assisted casting. A 4×4 cell for the specimens was first created using an Ultimaker 2 + Fused Deposition Modeling (FDM) 3D printer with ABS (Acrylonitrile Butadiene Styrene) as the material. The printed ABS shapes were placed in a cardboard box, and Poly-Sil PS 8510, a two-component silicone rubber, was mixed in a 1:1 ratio and poured into the box. After curing at room temperature for at least one hour, the silicone rubber hardened and was removed from the cubic box. Finally, the cementitious materials were cast into the silicone rubber mold (Fig. 1d). Once the cementitious materials harden, these silicone rubber molds are easy to demold and durable enough for repeated use. Note that the actual mold dimensions may vary within 0.8 mm from the design parameters due to printing quality and the use of a 0.8 mm nozzle.

The mixture proportions of the ACCCs, detailed in Table 2, were tailored based on a previous study including CEM I 42.5 N, fly ash, sand (125–250 μm grain size), water, polycarboxylate superplasticizer, viscosity modifying agent (VMA), and Polyvinyl Alcohol (PVA) fiber. A fine-grained fiber reinforced mortar served as the constituent material, with PVA fiber from Changzhou TianYi Engineering Fiber used as reinforcement at a 2 % volume fraction, as shown in Table 3. Methylcellulose powder from Shanghai Ying Jia Industrial Development Co. Ltd. was employed as a viscosity modifying agent (VMA) to enhance fiber distribution. MasterGlenium 51, a polycarboxylate-based superplasticizer by BASF (Germany), was utilized to achieve the desired workability. A water-to-binder ratio of 0.46 was chosen to ensure proper casting of the cement materials into the small mold, promoting good fluidity. The dry ingredients, which included CEM I 42.5, fly ash, sand, and VA, were mixed together using a Hobart machine for a duration of four minutes. Following this, water and superplasticizer were introduced into the dry mixture, and an additional mixing period of 2 minutes ensued. Subsequently, the fibers were slowly incorporated into the mortar and mixed for an additional 2 minutes. To ensure uniform distribution of the fibers within the matrix, a high-speed rotation was applied for an additional 5 minutes. The fresh paste was then poured into silicone molds, filling each mold in two layers. Each layer underwent 20 seconds of vibration to ensure proper consolidation and uniform fiber distribution. Finally, plastic films were applied to cover the molds, preventing evaporation. After three days of curing at room temperature, the specimens were transferred from the molds to a curing chamber (20℃, 96 % RH) until they reached 28 days. Then, they were removed from the chamber, and a cutting machine was used to divide the 4×4 cell specimen into four 2 × 2 cell specimens. The cutting lines on the specimens are shown in white in Fig. 1d. The constitutive material properties under uniaxial tension and uniaxial compression [35] are shown in Fig. 2.

2.2. Multiple impact tests

For a cellular geometry with small dimensions, an impact test with specific impact energy similar to the drop-weight impact test was performed using a Schmidt hammer OS-120PM as an impactor, as shown in Fig. 3. The Schmidt hammer OS-120PM (Figs. 3a, 3b) is commonly used for assessing the compressive strength of low strength mortar through low-velocity impact tests. The fundamental principle of the Schmidt hammer involves the energy balance between the elastic energy stored in its springs and the energy absorbed or dissipated upon impact with

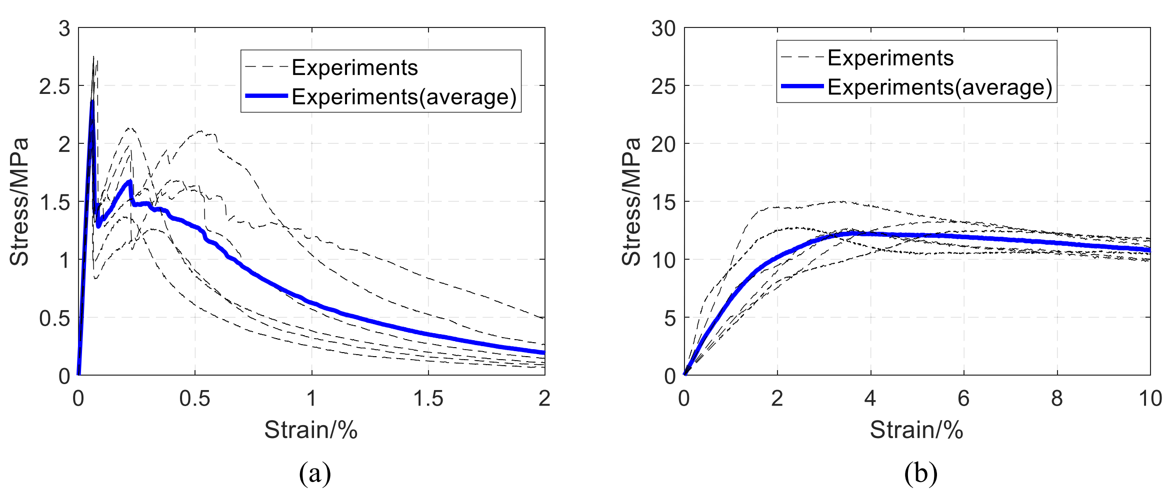

Fig. 2. Constitutive material properties, (a) uniaxial tension, (b) uniaxial compression.

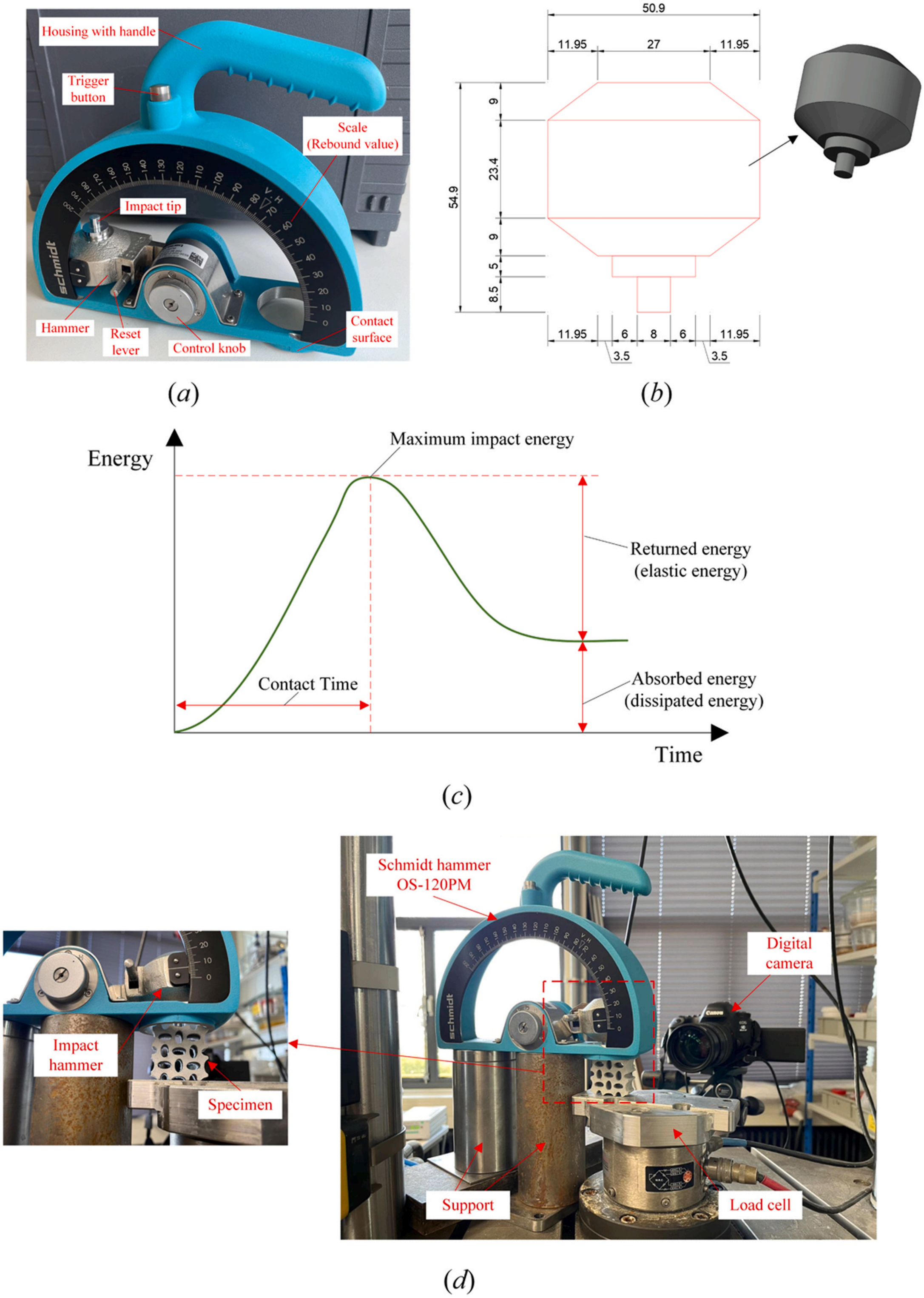

Fig. 3. Schmidt hammer OS-120pm (a) and its impact hammer head with measured dimensions (b), the energy absorption process using the impact hammer as an impactor (c), experimental setup for multiple impact tests (d).

tested specimens. As shown in Fig. 3c, when the hammer impacts a specimen, the specimen's received energy initially rises with contact time, peaks at maximum energy as the impactor begins to rebound, and eventually stabilizes when the impactor loses contact with the specimen. This stabilized value represents the absorbed energy of the specimen. For the Schmidt hammer OS-120PM, each single impact delivers 0.833 J of kinetic energy to the surface of the tested specimen via the impact tip with measured dimensions in Fig. 3b. Prior to impact, the spring is preloaded to a fixed original position, denoted as $x_0 = 75$. Following impact on the specimen surface, the impact tip rebounds to another position, denoted as R, which is recorded as the rebound value of the impact (returned energy to the hammer [42] in Fig. 3c). The rebound value also serves as an indicator of the elastic energy returned by specimens after each impact (refer to Fig. 3c). A higher rebound value

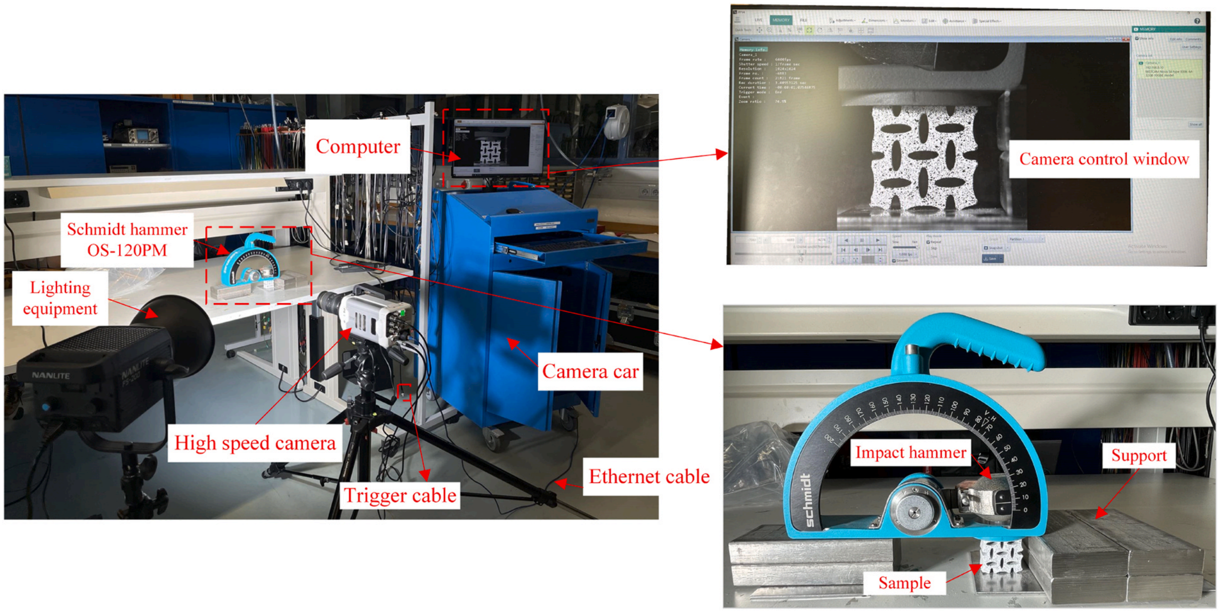

Fig. 4. Impact test setup using high-speed camera.

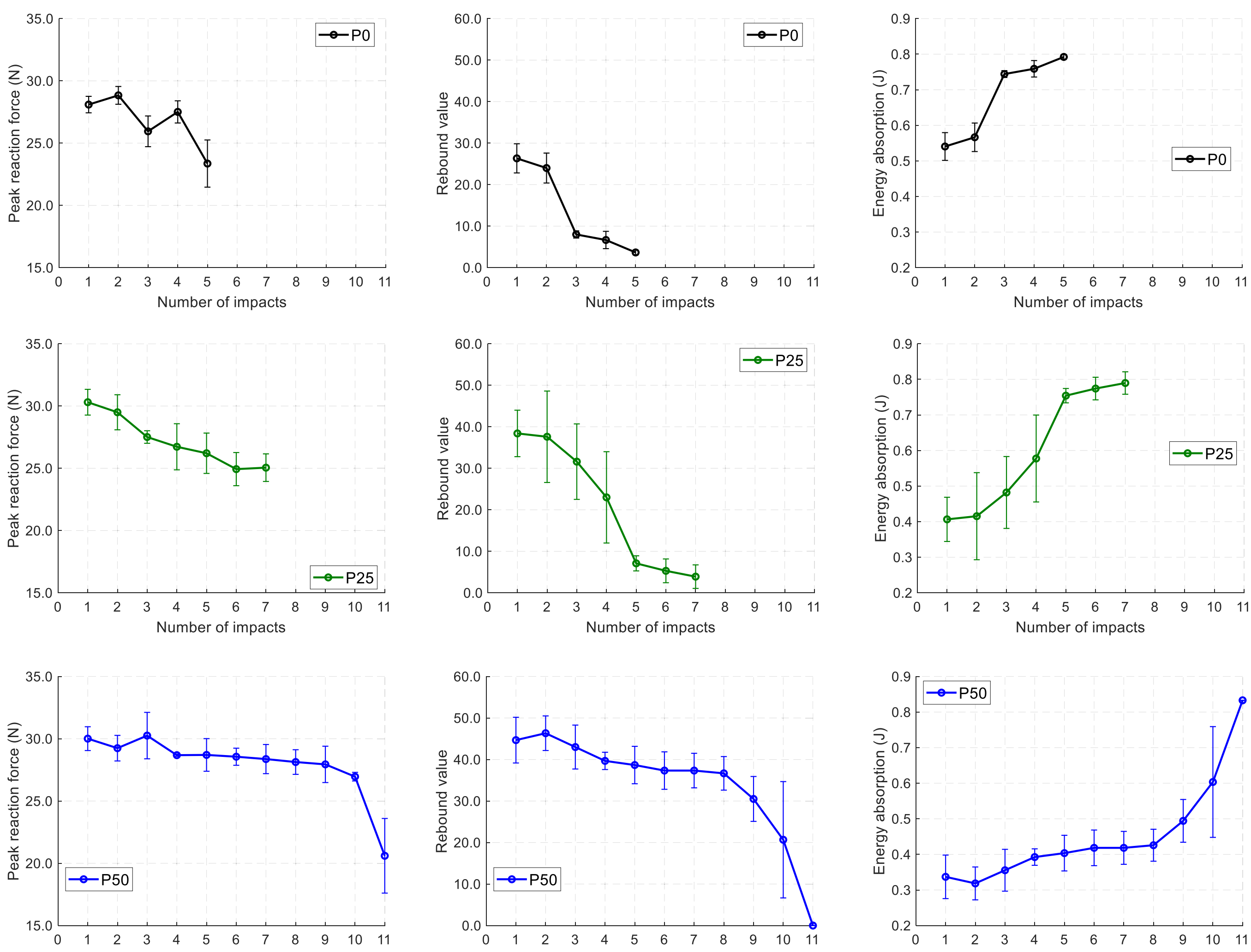

Fig. 5. Multiple impact test results of the three specimens.

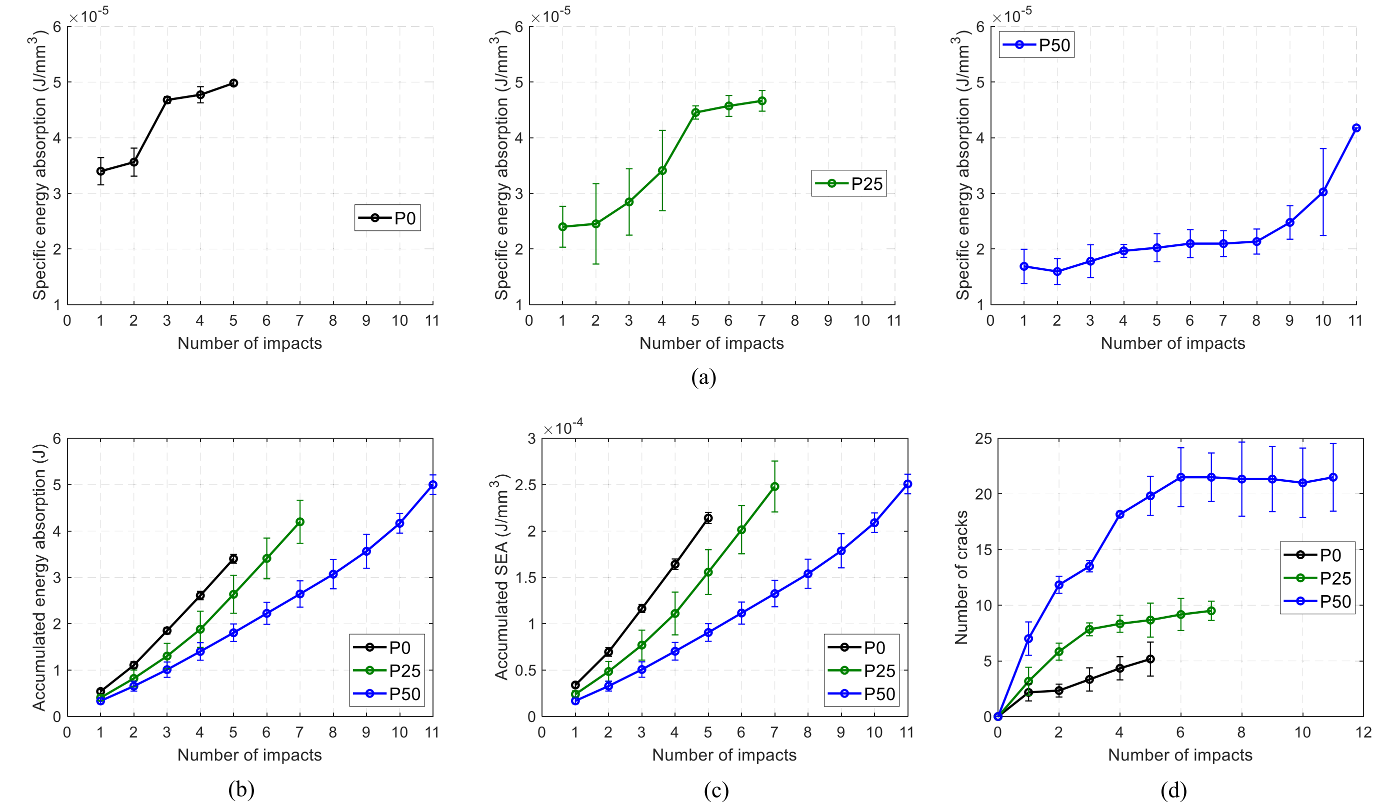

Fig. 6. (a) Specific energy absorption of specimens, (b) accumulated energy absorption through multiple impacts, (c) accumulated specific energy absorption through multiple impacts, (d) number of cracks versus number of impacts.

indicates that a larger portion of the impact energy is returned to the hammer. This indicates that the specimens retain greater elasticity and experience less localized damage in the impact zone and less plastic dissipation throughout the structure. When the rebound value approaches zero, it means the specimen has absorbed all impact energy through local damage in the impact zone and plastic dissipation throughout the structure, leaving no elastic energy to return the hammer. Ignoring energy dissipation via heat and sound, the energy absorbed by the specimen, denoted as E, can be expressed by Eq. (1).

$$E = \frac{x_0 - R}{x_0} * E_0 \tag{1}$$

where E_0 is the initial kinetic impact energy. For the Schmidt hammer OS-120PM, E_0= 0.833 J.

Fig. 3d illustrates the experimental setup for conducting multiple impact tests on the specimens. The specimens were positioned on the load cell of Instron 8874, which recorded the reaction force during each impact. A digital camera was utilized to capture the crack pattern of specimens after each impact, covering both the front and back sides of the specimens. Supports were assembled to ensure alignment of the top surface of the specimens with the bottom surface of the impact tip (Fig. 3a) of the Schmidt hammer head. During the first impact, the impact tip is adjusted to strike the center of the specimen's top surface. Before the next impact, it is ensured that the impact tip strikes the same position on the specimen as in the previous impact. At least three replicates were tested for each shape to obtain reliable results.

2.3. Strain analysis using high-speed DIC

Similar to the impact test setup depicted in Fig. 3d, an impact test setup utilizing a high-speed camera is illustrated in Fig. 4. The high-speed camera employed was the Photron FASTCAM Mini AX200, capable of capturing images at a resolution of 1 megapixel (1024x1024 pixels) with a frame rate of 6400 fps (frames per second). The high-speed camera was connected to the camera car through an Ethernet cable and controlled by a computer. Lighting equipment was used to illuminate the specimens during impact loading. The testing procedure commenced by starting recording in the computer controlling the high-speed camera, then triggering the Schmidt hammer impact, and terminating the recording using the trigger cable. The "end" trigger mode was used with a record duration of 3.41 seconds, meaning the content from the last 3.41 seconds before the trigger is recorded. Subsequently, a brief segment of the impact process was chosen and extracted from the recorded duration for subsequent DIC analysis. Additional information is available in the videos provided in the Supplementary data. Only the initial impact was considered in DIC analysis, as the specimens already exhibited damage prior to the second impact.

Supplementary material related to this article can be found online at 10.1016/j.conbuildmat.2025.140692.

Supplementary material related to this article can be found online at 10.1016/j.conbuildmat.2025.140692.

Supplementary material related to this article can be found online at 10.1016/j.conbuildmat.2025.140692.

2.4. Results and discussion

2.4.1. Impact resistance

Fig. 5, Fig. 6a compare the impact results for specimens P0, P25, and P50 regarding the peak reaction force, rebound value, energy absorption and specific energy absorption (SEA) during multiple impacts. Figs. 6b, 6c illustrate the accumulated energy absorption and specific accumulated energy absorption (SEA) through multiple impacts for the three specimens. Further crack propagation for these specimens are shown in Fig. 6d, Figs. 7–10. Fig. 5 shows a decrease in the rebound value for all specimens as the number of impacts increases, caused by the accumulation of local damage in the impact zone and plastic dissipation

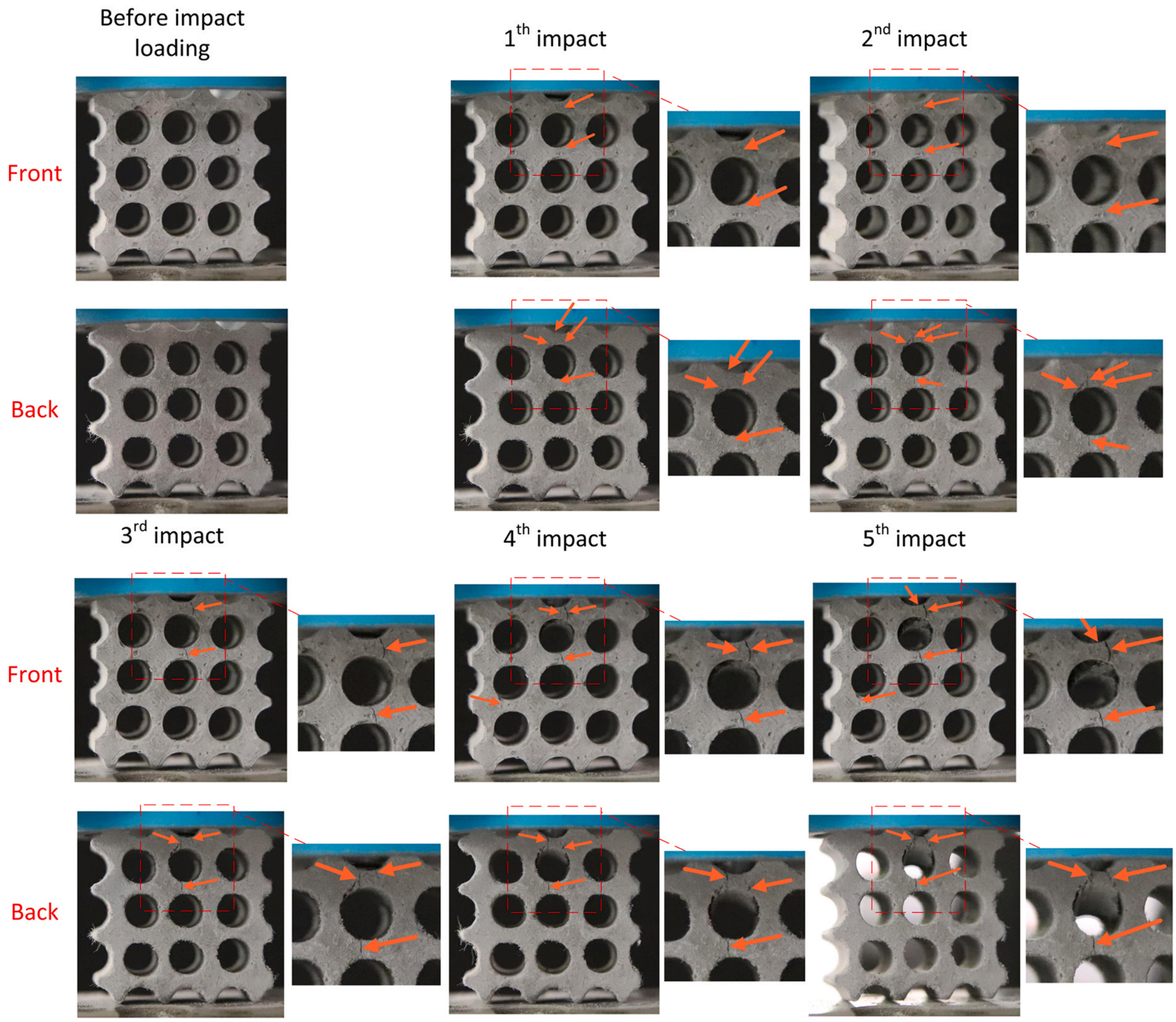

Fig. 7. Crack propagation of P0 during multiple impacts.

throughout the structure. Similarly, energy absorption of the specimens due to the local damage and plastic dissipation rises with the growing number of impacts, inversely proportional to the rebound value. Among the specimens, P50 demonstrates the highest impact endurance, enduring up to 11 impacts before reaching local failure in the impact zone. Subsequently, P25 can withstand 7 impacts before the local failure, while P0 can only endure 5 impacts before reaching complete damage in the impact zone. From the initiation of impact until the specimens fail in the impact zone, P50 showcases a slower progression of the local damage, while P25 displays a faster rate of the local damage, and P0 demonstrates the quickest rate of the local damage. As depicted in Fig. 5, following 2 impacts, P0 exhibits a rapid rate of the local damage. Similarly, P25 also demonstrates a swift rate of the local damage after 2 impacts, albeit slower than P0. Conversely, P50 exhibits a notably slower rate of the local damage compared to both P0 and P25. In Fig. 6a, the specific energy absorption (SEA) of the three specimens was calculated to remove the influence of material volume on energy absorption during multiple impacts. Despite this adjustment, the observed trends remain consistent with those noted earlier. In Fig. 6b, P0 demonstrates the minimum accumulated energy absorption of 3.4 J among the three specimens after the fifth impact upon failure. ACCCs specimens P25 and P50 exhibit higher accumulated energy absorption until failure than P0. Specifically, P25 shows an accumulated energy absorption of 4.2 J after 7 impacts upon failure. Among the three specimens, P50 achieves the maximum accumulated energy absorption of 5 J after 11 impacts upon failure. Fig. 6c reflects a similar trend in accumulated SEA until failure. Although P0 is the lightest, its accumulated SEA until failure is still lower than that of the ACCCs specimens. Since P25 is lighter than P50, its accumulated SEA until failure is closer to that of P50.

It can be found from Fig. 5 that the peak reaction force decreases with an increasing number of impacts for all specimens until they reach failure in the local impact zone. The reason can be explained as follow: the tensile behavior of the cementitious material matrix used in this research has been tested in our previous study [35] and is shown in the modelling section. Following the elastic phase in the tensile behavior, a single crack emerges, and subsequent plastic deformation due to fiber-bridging within the crack is limited to sustain minor stress. As the impacts accumulate, the specimens absorb more impact energy through plastic deformation and the local damage. Given that the impact energy remains constant for each impact, the specimens' elastic strain energy diminishes, reducing their ability to sustain and transfer force to the bottom plate. The peak reaction force is closely related to the contact stiffness of specimens [43]. As the local damage occurs and contact stiffness decreases, the peak reaction force diminishes. P0 suffers severe the local damage in their impact zone with consistent impact energy per impact. This reduces the elastic strain energy available to rebound the hammer, decreasing the impact force transmitted to the bottom plate. In contrast, ACCCs specimens display a higher peak reaction force during impact due to their auxetic behavior. This behavior facilitates the

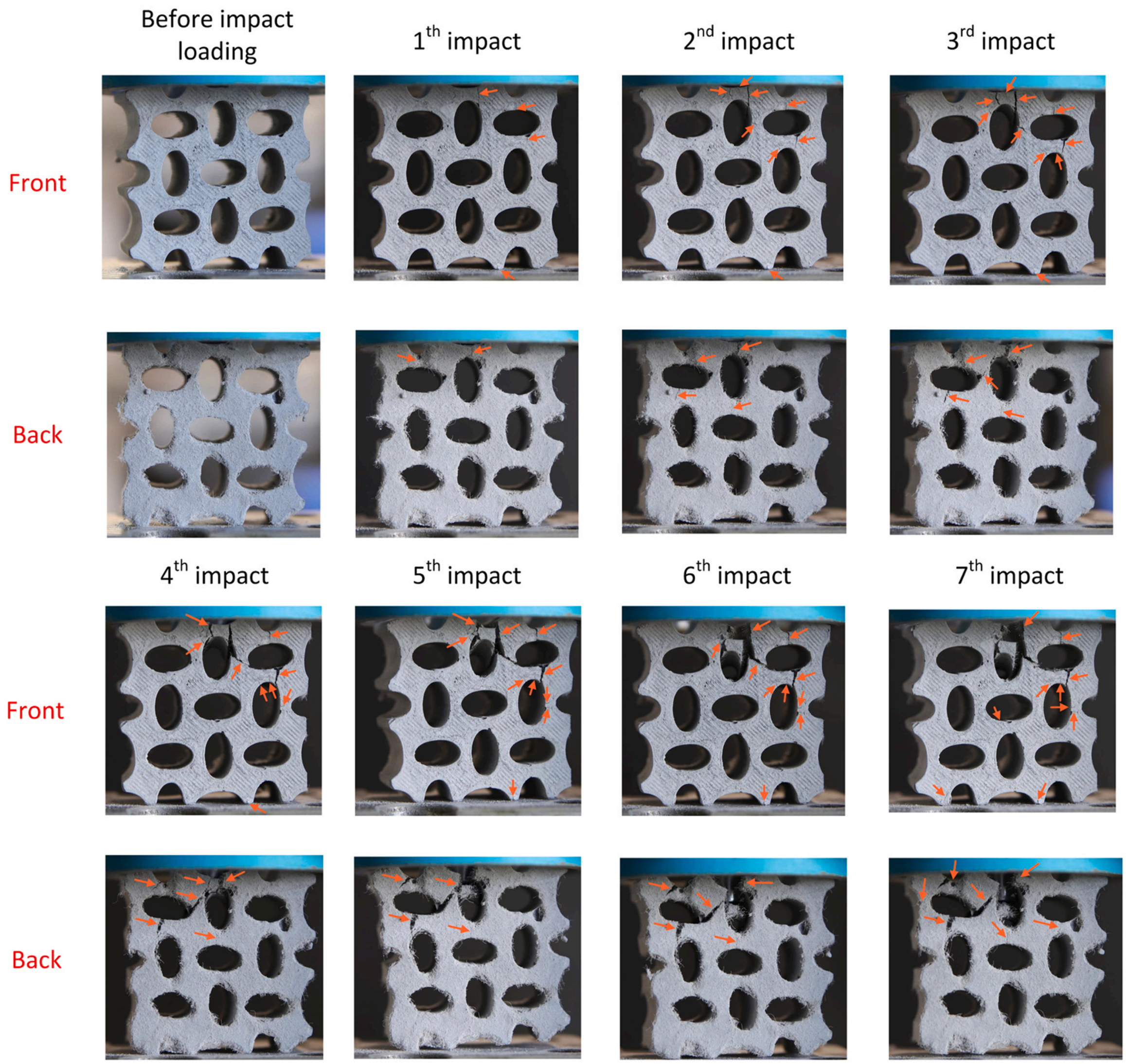

Fig. 8. Crack propagation of P25 during multiple impacts.

contraction of the structure upon impact through the rotation of sections (see in Fig. 1, as defined in our previous study [41]) and inward folding around fiber-bridging cracks within the ligaments. Consequently, material concentration beneath the impact zone enhances the local stiffness of the auxetic structure. The impact energy within the zone is mitigated by distributing it to other parts of the specimen. Similar to the energy absorption for the impact energy, P50 continues to exhibit greater localized stiffness by demonstrating a higher peak reaction force compared to P25.

The error bar observed in Fig. 5 can be attributed to several factors: (1) Due to errors in additive manufacturing and cutting tolerances of the cutting machine, there are variations among the four joints at the bottom of the specimens. This results in incomplete and uneven contact with the loading plate prior to impact. (2) It is difficult to maintain a precise impact at the exact center of specimens along their thickness direction; (3) the heterogeneity of the cement-based material.

2.4.2. Crack propagation during multiple impacts

Fig. 6d shows the changes in the number of cracks observed in the specimens during multiple impact tests. Their progression of crack propagation during multiple impacts are depicted in Figs. 7–9, with cracks indicated by orange arrows. Here, "Front" denotes the front side of the specimen, while "Back" indicates the back side. Crack propagation was monitored on both sides of the specimens due to the heterogeneity of cement-based materials, and the average number of cracks from both sides was recorded as the number of cracks developed during each impact in Fig. 6d. As the number of impacts increased, all specimens exhibited a greater number of cracks, which widened over time. In later stages, certain cracks within the specimens began to interconnect and perforate, leading to localized damage. During multiple impacts, P0 primarily exhibits localized cracks, which are concentrated in the central ligaments near the impact area. The axial impact load causes P0 to separate on both sides around the impact zone, resulting in a significantly lower contact hardness. After the third impact, the rebound value of P0 significantly dropped to below 10, and the impact energy absorption through the local damage reached 89.3 %. This suggests that localized material failure with crack penetration had occurred. Consequently, P0 has the fewest cracks. In contrast, P25 and P50 display a greater number of cracks distributed along the ligaments connecting adjacent holes, spreading over a larger area of their structure. These ligaments with fiber-bridging cracks tend to function as joints, facilitating section rotation and inward folding, thereby inducing auxetic behavior. This auxetic behavior allows the impacted area to remain densely packed, reducing local damage while redistributing the impact energy through plastic deformation in other parts of the structure. As a result, ACCCs specimens maintain relatively good contact stiffness, which explains their higher peak reaction force during multiple impacts, as shown in Fig. 5. However, with each impact, local damage

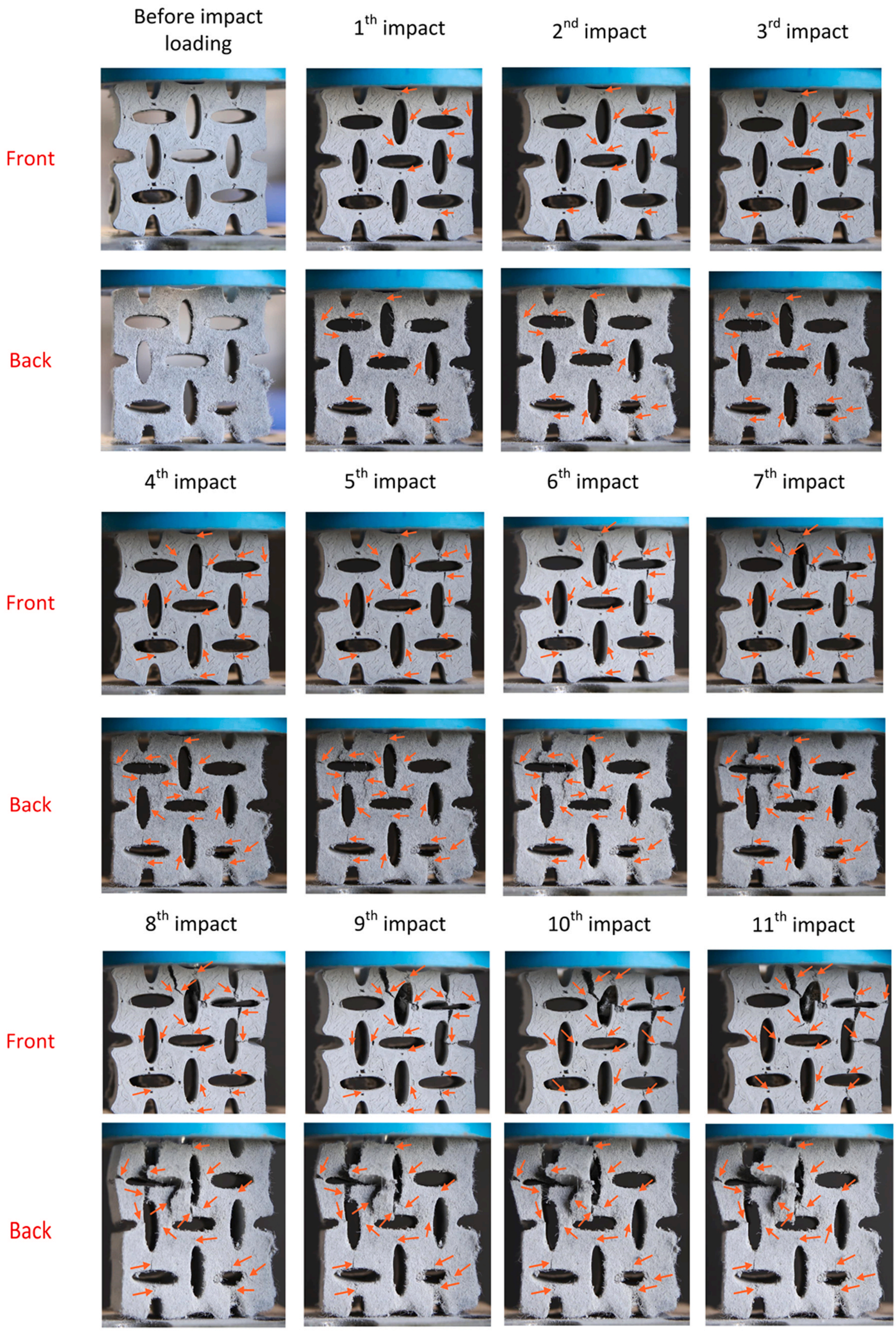

Fig. 9. Crack propagation of P50 during multiple impacts.

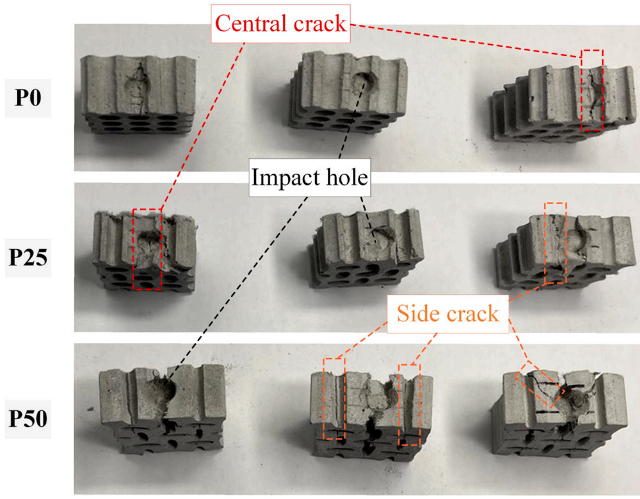

Fig. 10. Crack distribution across specimen thickness upon failure after multiple impacts.

progressively increases due to greater plastic deformation in the ligaments, widening of existing cracks, and material loss in the impact zone. Eventually, the contact stiffness decreases until localized failure occurs due to crack penetration and linkage. After the fifth impact, the rebound value of P25 significantly drops to below 10, with a plastic energy dissipation approaching 90.5 %, indicating localized failure resulting from crack penetration and linkage. In contrast, P50 exhibits enhanced damage tolerance and stronger impact resistance by developing more cracks throughout the whole structure, with localized failure occurring only after the eleventh impact. This superiority is attributed to the greater magnitude of the negative Poisson's ratio in P50 compared to P25 before self-contact within their central elliptical-shaped holes, as determined in the uniaxial compression test in our previous study [41]. The negative Poisson's ratio, being proportional to the volume of material drawn under the impact zone, proves effective in mitigating localized impact damage. As seen in Figs. 7–9, P50 disperses cracks more extensively throughout the specimen compared to P25. This is attributed to the greater auxetic behavior of P50, which facilitates the transfer of impact energy to other parts of the specimen.

Fig. 10 shows the crack distribution of the specimens along their thickness direction upon failure after multiple impacts. The hammer tip, with an 8 mm diameter, was applied to specimens that are 20 mm thick. In Fig. 10, an impact hole was observed in the middle of the top surface of each specimen, with the central area exhibiting more severe damage or perforation compared to the sides. Still, P0 only shows cracks in the center of its top impact surface. In contrast, ACCC specimens display both central and side cracks on their top surface, demonstrating a superior ability to distribute impact energy across different parts of the specimen.

2.4.3. Strain analysis during impact duration

To analyze the major strain distribution during the initial impact, the condition of the specimens captured by the most recent frame before the impact was regarded as the initial state (i.e., 0 μs in Figs. 11–13). The time internal was set as the time per frame recorded by high-speed camera (i.e., 156.25 μs). Figs. 11–13 illustrate the changes in major strain distribution across all specimens during the duration of contact time under the initial impact loading. To enhance the visualization of the major strain distribution in Figs. 11–13, a strain range of 0.006–0.03 was selected to clearly depict the microcrack distribution and damage modes. Strains above 0.03 are highlighted in red, while those below 0.03 are shown in dark blue. The sudden application of force upon impact slightly impairs the effectiveness of Digital Image Correlation (DIC) at the moment of 156.25 μs. As the contact time increases, the occurrence of major strain in the ligament gradually increases and further intensifies. The variations in major strain distribution among the three specimens remain relatively minor after 625.00 μs for the initial impact. It can be found that the significant major strain in ACCC specimens, namely P25 and P50, primarily disperses along the ligaments connecting adjacent holes across a significant portion of the structure. This indicates that ACCC specimens display a ductile damage mode, where cracks develop and spread to various locations throughout the contact duration during impact loading. In our prior research [33], the auxetic effect exhibited by ACCCs specimens arises from the lateral inward movement of unit cells, triggered by their rotation and inward folding under uniaxial compression. Likewise, the ligaments with the significant major strain tend to act as joints, promoting section rotation and inward folding under impact loading, thereby inducing auxetic behavior. This leads to the engagement of surrounding material into the impact zone, facilitating the efficient transfer of the impact energy throughout the structure. Specially, the significant major strain of P50 extends across

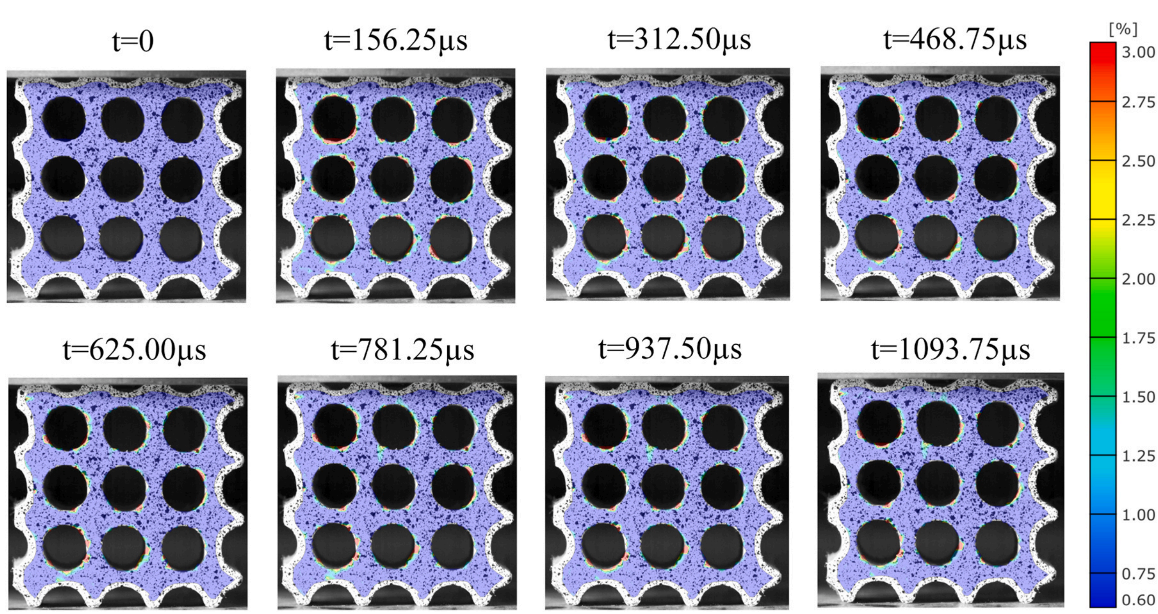

Fig. 11. Major strain of P0 during initial impact.

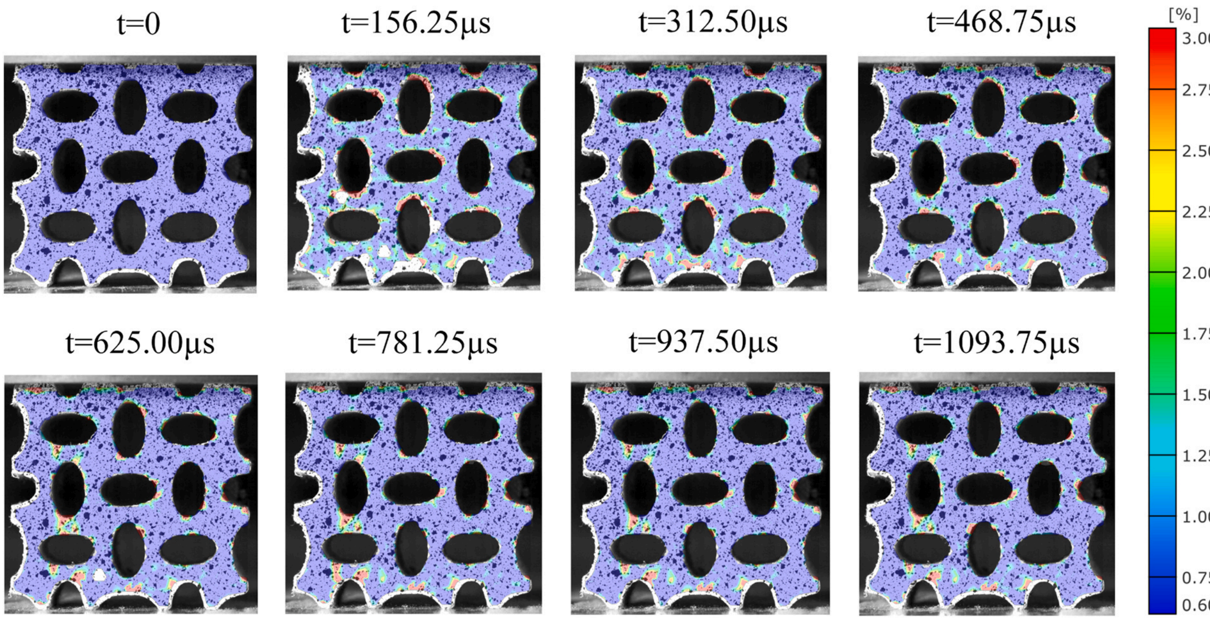

Fig. 12. Major strain of P25 during initial impact.

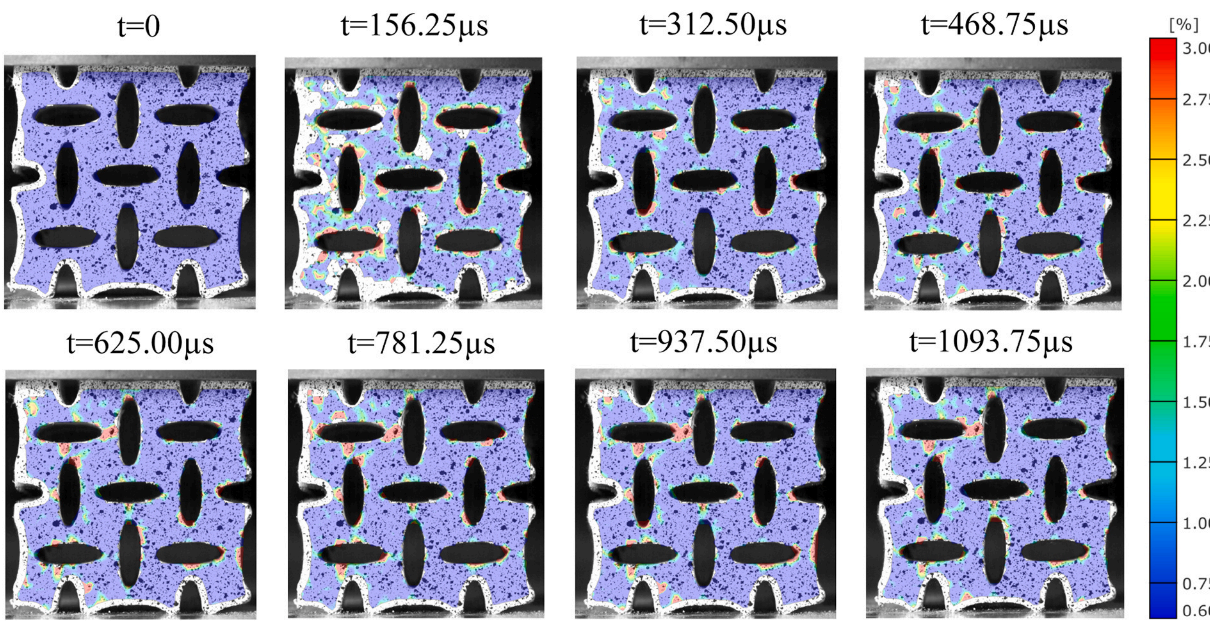

Fig. 13. Major strain of P50 during initial impact.

more ligaments compared to P25, and it is also more evenly distributed. This also explains the stronger impact resistance for P50 during multiple impacts in Fig. 5. Conversely, the significant major strain of P0 is concentrated in the middle ligaments near the impact zone. This indicates that P0 exhibits a brittle damage mode, characterized by the immediate formation of cracks near the impact zone, with no subsequent crack development to facilitate energy dissipation. Due to the structural configuration of P0, which does not promote auxetic behavior triggered by section rotation around ligament cracking. Consequently, the impact energy cannot effectively transfer to other regions of the structure, resulting in localized damage. Due to the brittleness and heterogeneity of cementitious materials, considerable strain from impact-induced stress concentration was observed around the holes in all specimens.

$$\upsilon = -\frac{\varepsilon_x}{\varepsilon_y} \tag{2}$$

The variations in compressive and lateral strain during the initial impact were analyzed using Digital Image Correlation (DIC) and illustrated in Fig. 14. In uniaxial compression tests, specimens are typically placed between two plates and undergo uniform compressive deformation, allowing for easy calculation of Poisson's ratio using Eq. (2). However, in the impact scenario studied here, localized impact is applied to the specimen, resulting in uneven compressive deformation. Hence, compressive and lateral strains of each specimen were indirectly used to evaluate its Poisson's ratio during the impact. In Fig. 14a, the vertical distance between the two red points marked on each specimen was utilized to quantify its compressive strain or y-direction strain during the impact. Similarly, the horizontal displacement between the

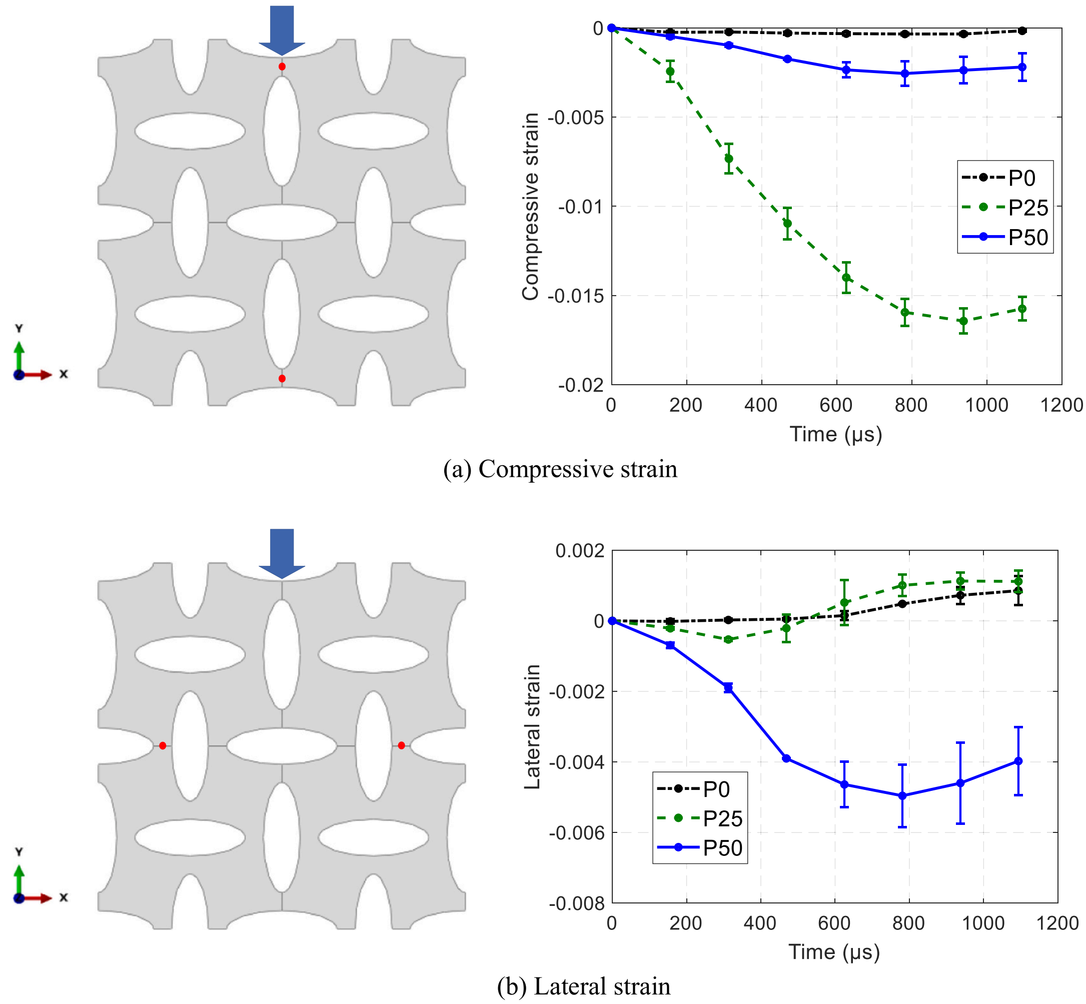

Fig. 14. Variations of compressive strain and lateral strain during initial impact analyzed by DIC.

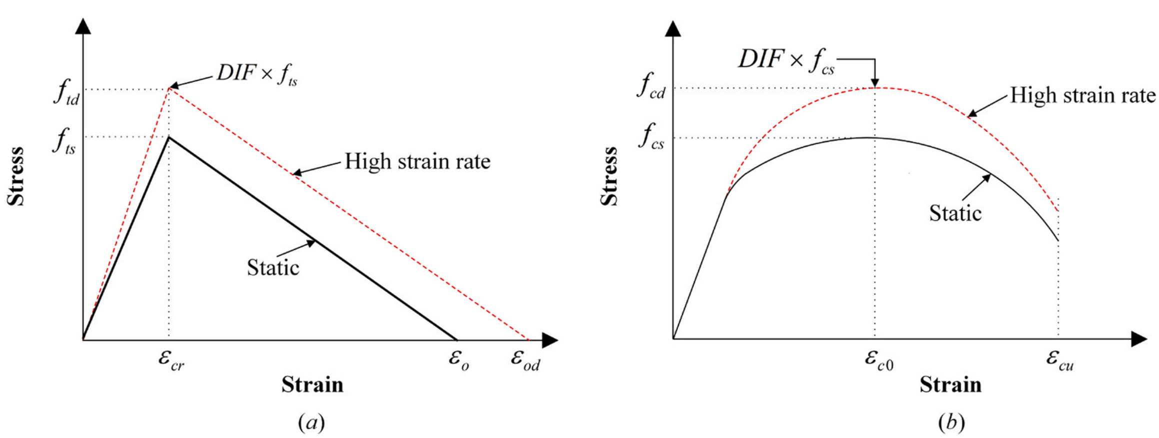

Fig. 15. Mechanical behavior of concrete subjected to static and impact loading, (a) tension (b) compression.

two red points marked on each specimen in Fig. 14b was utilized to quantify its lateral strain or strain in the x-direction during the impact. It is observed that all specimens exhibit an increase in compressive strain, stabilizing at the end of the contact time. ACCC specimens demonstrate higher compressive strain than specimen P0 due to their greater compressive deformation. Specifically, P25 exhibits higher compressive strain, with a maximum magnitude of 1.64 %, compared to P50, which has a maximum magnitude of 0.26 %. This arises from the larger compressible space and lesser cementitious matrix material in P25. In Fig. 14b, P0 consistently shows positive lateral strain, indicating expansion of the structure during the impact. As the impact on P0 is localized, the overall structure undergoes minimal deformation during the impact, resulting in the smallest magnitude of lateral strain. Conversely, ACCC specimens exhibit negative lateral strain, indicating contraction of the specimen during the impact. P25 initially presents negative strain (contraction behavior) with a maximum magnitude of

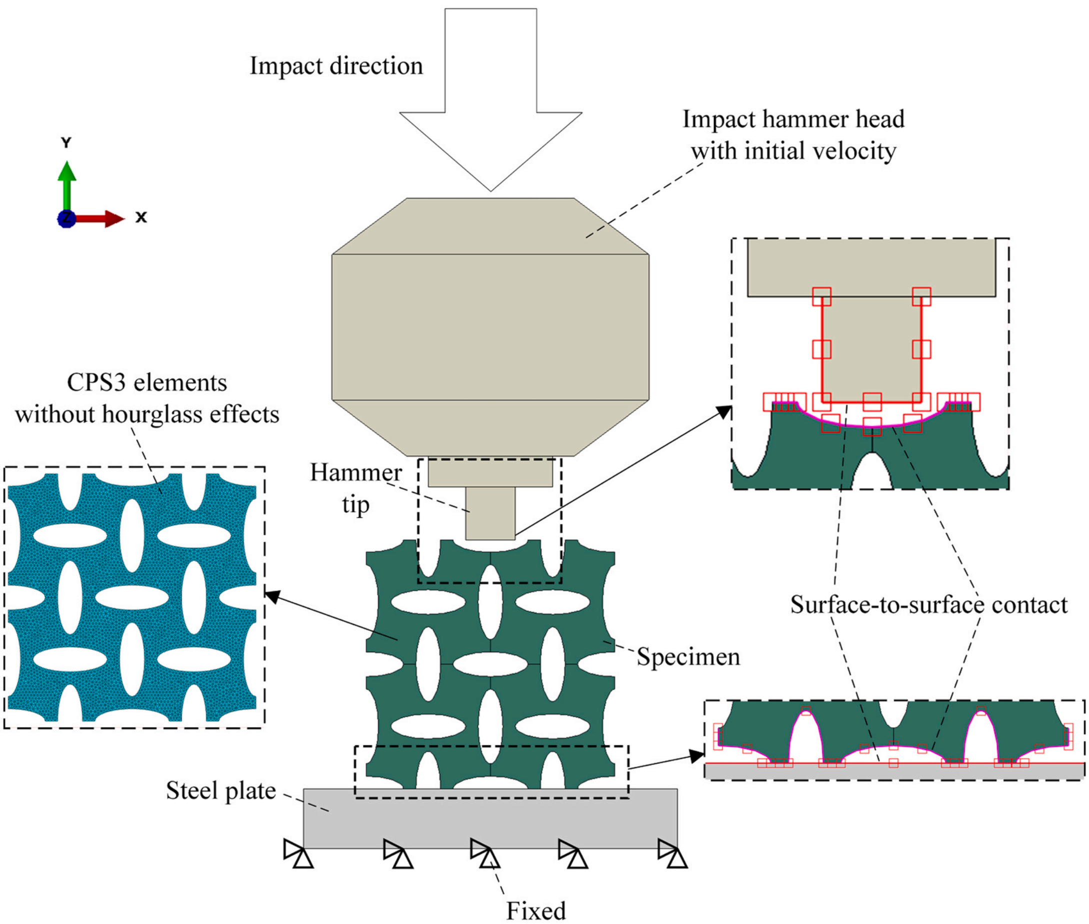

Fig. 16. Modelling of ACCCs subjected to impact loading.

Table 4
CDP model parameters for ACCCs.

ρ_{aux}(kg/m^3)	E_0(MPa)	ν	σ_{b0}/σ_{c0}	K_c	ψ	ε_{ec}	Viscosity Parameter
1870	3997	0.2	1.16	0.667	35	0.1	0.001

Table 5
Tensile behavior parameters.

Yield stress (MPa)	Displacement (mm)
2.358	0
1.283	0.0519
1.671	0.180
1.477	0.265
1.235	0.505
0.959	0.669
0.641	0.962
0.334	1.551
0.193	1.995

0.05 %, which transitions to positive strain (expansion behavior) after about 156.25 μs. In contrast, P50 consistently shows negative lateral strain with contraction behavior, exhibiting a maximum magnitude of 0.54 %. According to Eq. (2), compared to P25, P50 demonstrates greater lateral strain and lower compressive strain, indirectly indicating a higher magnitude of negative Poisson's ratio and thus a greater auxetic behavior. Besides the factors discussed for the error bar in Fig. 5, the specimen's separation from the hammer at the final contact stage leads to a significant mechanical state change, contributing to a larger error bar in Fig. 14.

Table 6
Compressive behavior parameters.

Yield stress (MPa)	Inelastic strain
8.376	0
12.273	0.0158
12.027	0.0367
10.984	0.0765
10.586	0.0889
10.060	0.1264
9.948	0.1557
10.720	0.2030
11.333	0.2312

3. Numerical modeling

3.1. Simulation of ACCCs under impact loading

Given that impact loads can result in high strain rates within structures, it's imperative to account for the strain-rate dependent characteristics of cementitious materials. To simulate the progression of damage in cementitious specimens subjected to impact loading, the Concrete Damage Plasticity (CDP) model incorporating strain rate effects was employed [40,44–46]. Appendix B provides a concise overview of the CDP model. The material constitution in the CDP model only requires tensile behavior data from uniaxial tension tests and compressive behavior data from uniaxial compression tests. Yet the HJC (Holmquist-Johnson-Cook) model, Karagozian & Case (K&C) concrete

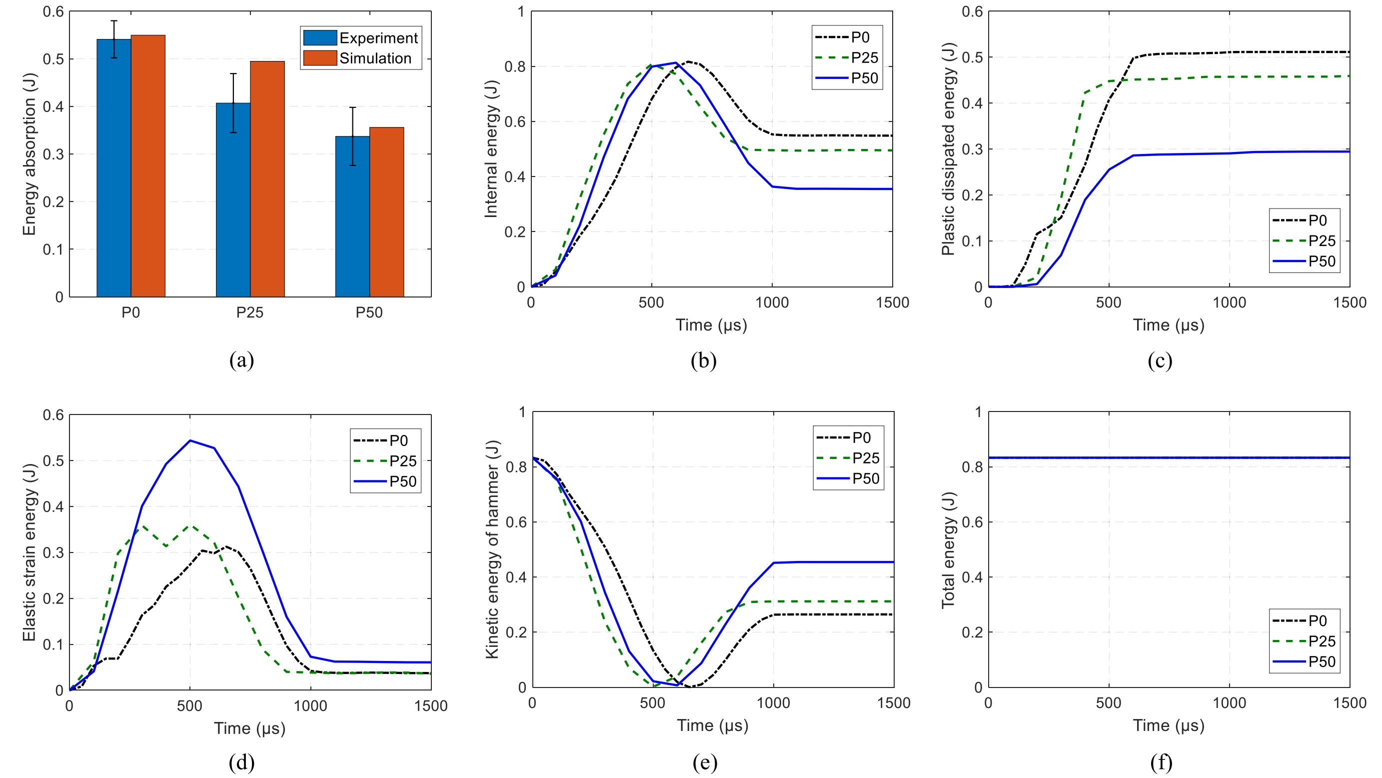

Fig. 17. Variations of different energies in the model during the initial impact test, (a) energy absorption of specimens after the initial impact, (b) internal energy of specimens, (c) plastic dissipated energy of specimens, (d) elastic strain energy of specimens, (e) kinetic energy of hammer, (f) total energy.

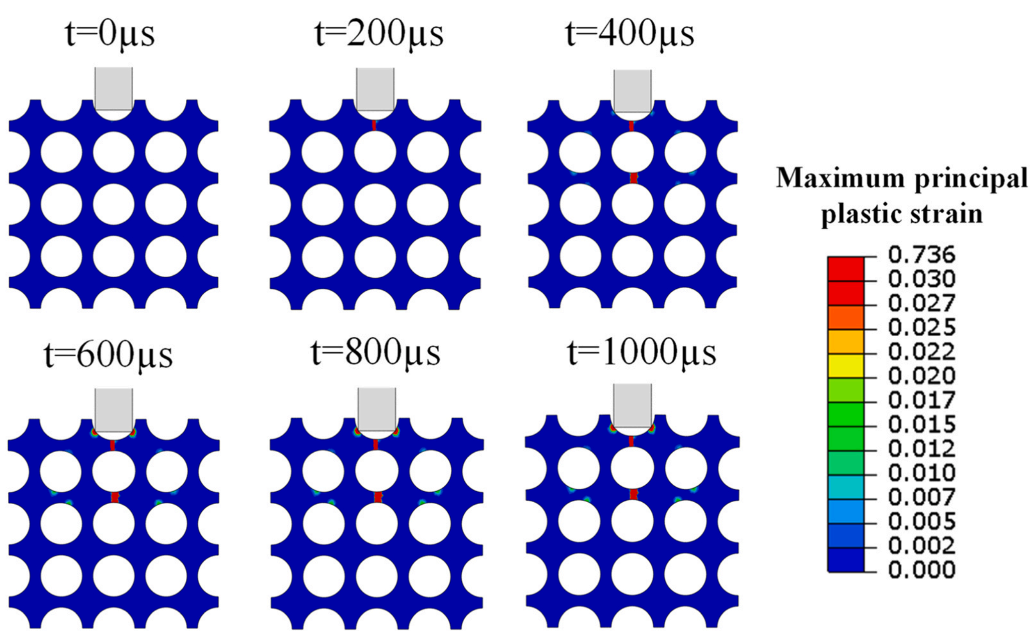

Fig. 18. Maximum principal plastic strain of P0 during initial impact in the model.

(KCC) model, ZWT model face notable limitations due to the determination of many parameters, which are obtained through complex experimental conditions. Appendix C provides a preliminary analysis of the three models applied to ACCCs. Typical stress–strain curves of concrete material under static and impact loading are depicted in Fig. 15, showcasing both compression (a) and tension (b) behaviors. In Fig. 15, f_{ts}, f_{cs} are the static tensile strength and compressive strength, respectively; f_{td}, f_{cd} are the dynamic tensile strength and compressive strength, respectively; ε_0, ε_{0d} are the static maximum tensile strain and dynamic maximum tensile strain, respectively; ε_{cu} is the maximum compressive strain, respectively; ε_{cr}, ε_{c0} are the peak tensile strain and peak compressive strain, respectively. The stress-strain behavior of concrete under impact loading demonstrates enhancement compared to that under static loading [47]. The strain rate effect on concrete-like material property can be characterized by comparing the dynamic and static values of material properties, typically quantified using the

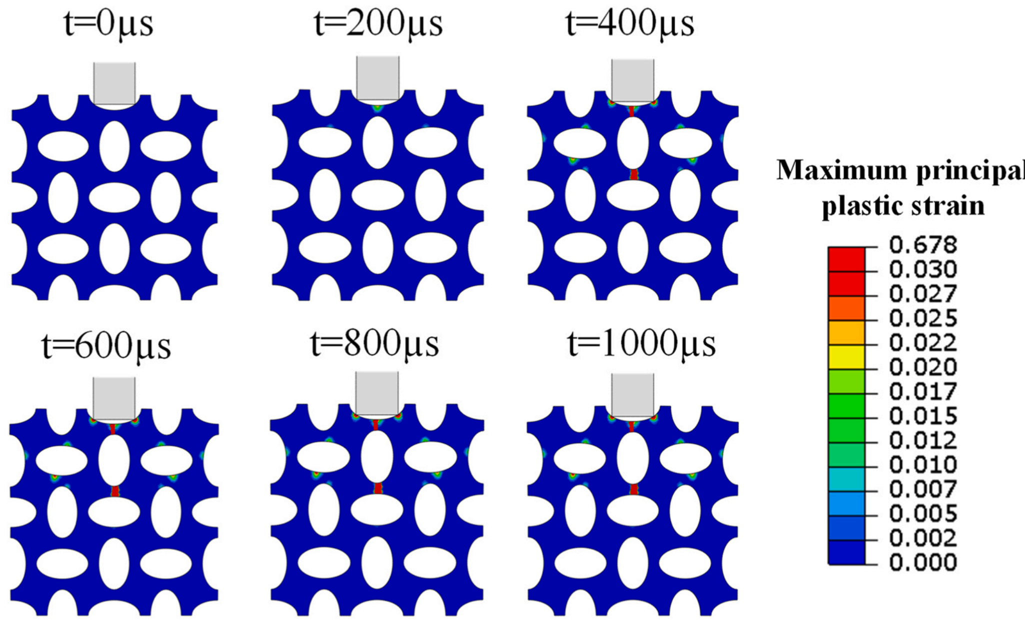

Fig. 19. Maximum principal plastic strain of P25 during initial impact in the model.

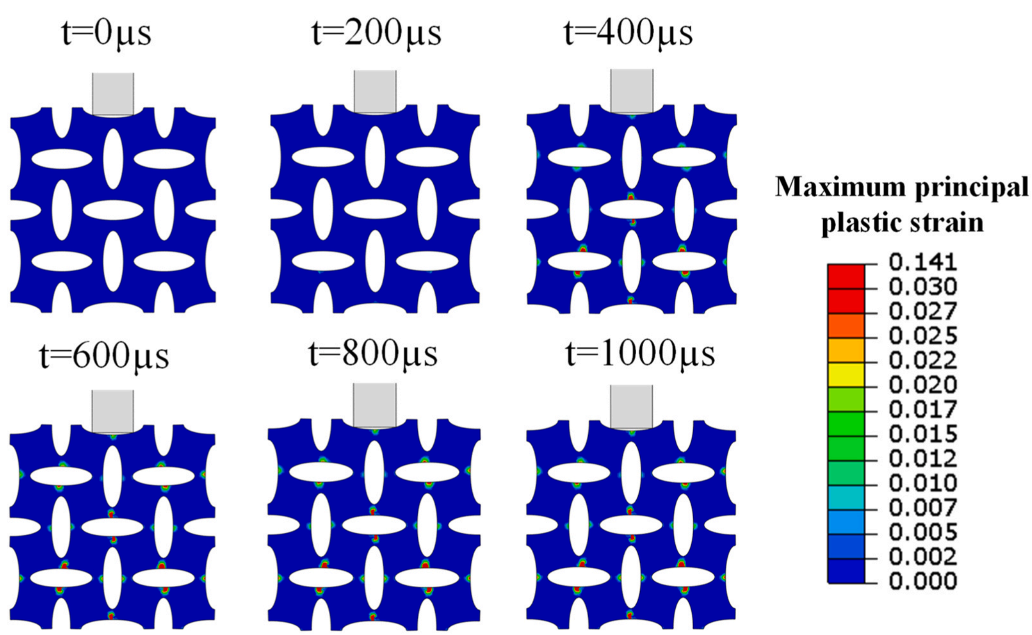

Fig. 20. Maximum principal plastic strain of P50 during initial impact in the model.

Dynamic Increase Factor (DIF). The DIF is calculated as the ratio of the dynamic property to the corresponding static property.

$$DIF = \frac{X_{dynamic}}{X_{static}} \tag{3}$$

The cementitious specimens have the same section along its thickness direction, which can be simplified to a 2D plane model. The impact hammer of Schmidt OS-120PM was considered as the impactor in the numerical modelling. The geometry of the impact hammer was also simplified to a 2D version based on its dimensions in Fig. 3b. The Schmidt OS-120PM impact hammer weighs 665 g and has a hammer head diameter of 8 mm. The initial kinetic impact energy of the Schmidt hammer OS-120PM is 0.833 J. To reduce computational time, the model of the hammer presented in the paper has been simplified to only include the hammer head. Treating the impact hammer head as a rigid body with uniform velocity, its initial velocity can be calculated as 1582.8 mm/s by accounting for its kinetic energy and mass. The impact mass is applied by specifying an equivalent density of the drop hammer head, calculated as the ratio of the total mass to the volume in the model. The initial velocity was applied to the impact hammer head by using a predefined field. To enhance computational efficiency, the drop hammer is positioned directly above the specimen's center, aligning the lower surface of the impact tip with the upper surface of the specimen. In the model, the impact tip has an 8 mm diameter for specimens P25 and P50. For specimen P0, the diameter of the impact tip was slightly reduced to 7.09 mm to accommodate the cylinder hammer tip's impact into the 8 mm width hole. This adjustment was made while maintaining the same hammer mass by modifying the density. The 7.09 mm taken in this model represented the equivalent side length of a square with the same area as the impact tip's circular surface area. This model was established

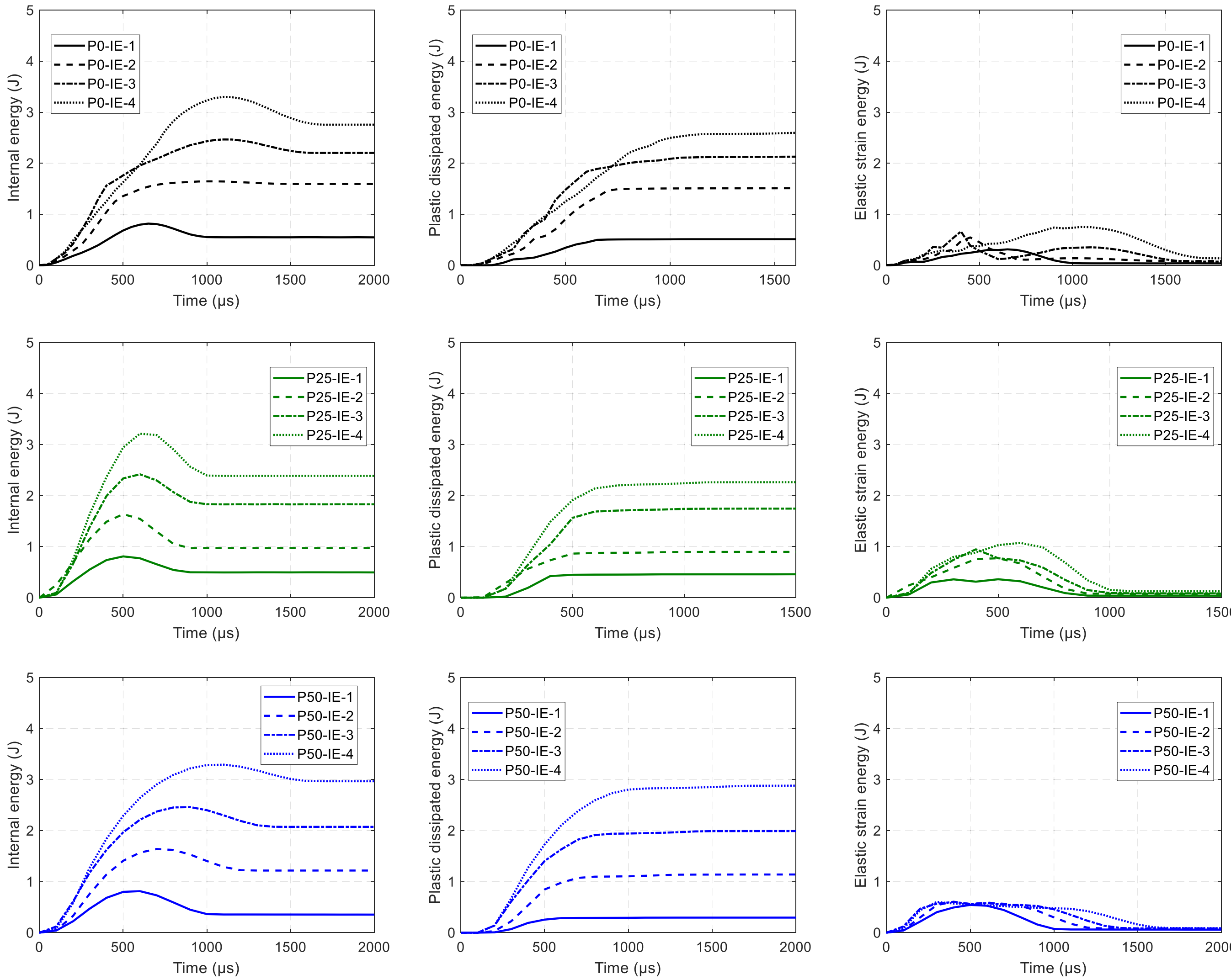

Fig. 21. Internal, plastic dissipated, and elastic strain energy of three specimens under different impact energies.

to investigate the energy absorption process during short-duration impact loading. Only the initial impact was considered in the model, as the specimens already exhibited damage prior to the second impact.

As shown in Fig. 16, an explicit dynamic Finite Element Method (FEM) model has been developed to simulate ACCCs specimens subjected to impact loading. In the explicit dynamic model, the energy time histories can be formulated as:

$$E_{Total} = E_K + E_I - E_W \tag{4}$$

$$E_I = E_e + E_p + E_a \tag{5}$$

where E_{Total} represents the energy balance for the whole model. E_K represents the kinetic energy. E_W represents the work done by the external loads. E_I represents the internal energy, comprising the sum of the recoverable elastic strain energy (E_e), energy dissipation due to inelastic deformation like plasticity (E_p), and artificial strain energy (E_a). The artificial strain energy E_a, used to control hourglass deformation, accounts for less than 1.0 % of the internal energy in the model in this research.

The CDP model considering strain rates effects was established in the explicit dynamics module of ABAQUS to simulate the impact behavior of ACCCs specimens under impact loading. The ACCCs specimen was meshed using CPS3 elements, which are 3-node linear plane stress triangular elements without hourglass effects. Table 4 gives the CDP model parameters for ACCCs specimens. In this table, ρ, ν, E_0 represent the density, Poisson's ratio, and initial elastic modulus of the cementitious matrix, respectively. Table 5 and Table 6 detail the material parameters of the CDP model, delineating the tensile and compressive behavior parameters for the cementitious matrix in static tests conducted in our previous study [35], respectively. The bottom plate in the model was modelled as a steel plate, consistent with the experimental setup, with an elastic modulus of 206 GPa, a Poisson's ratio of 0.3, and a density of 7800 kg/m^3. As depicted in Fig. 16, a surface-to-surface contact method was employed to establish the interaction between the impact hammer and cementitious specimens. In this model, friction was ignored between specimens and the hammer tip. To reduce the occurrence of overclosure or excessive mutual embedding in the normal direction, a hard contact approach was implemented between specimens and the hammer tip. The same surface-to-surface contact method was applied between specimens and the bottom plate. The bottom surface of the bottom plate was coupled with a reference point with fixed constraints.

In this study, the DIF of the tensile constitution is more significant than that of compression, as the auxetic behavior of ACCCs arises from tensile cracking in the ligaments. The data from existing literature about strain rate effects for concrete in tension indicates that the dynamic increase factor (DIF) follows a bilinear trend concerning the strain rate when plotted on a log-log scale. Specifically, there are no increments

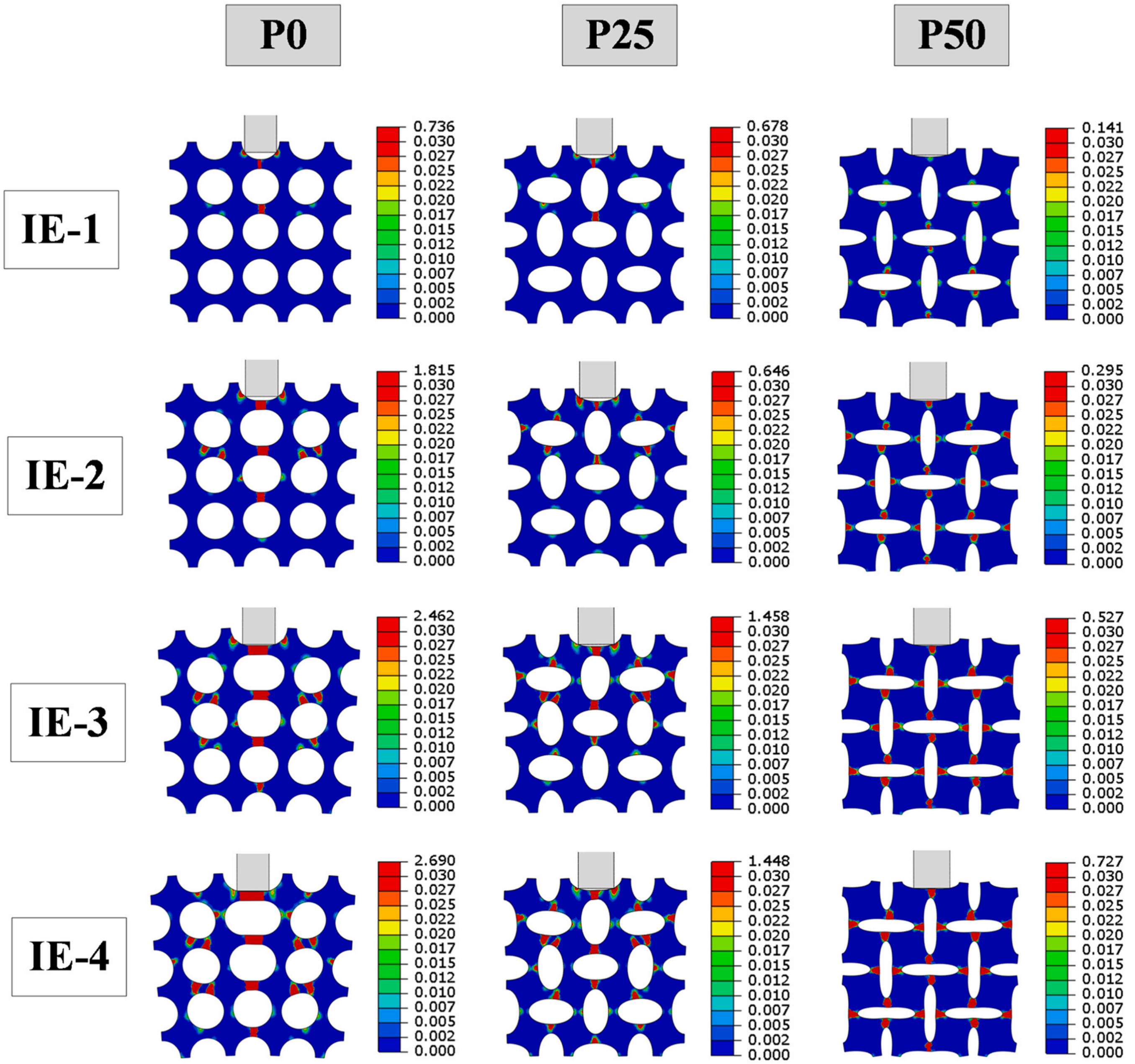

Fig. 22. Maximum principal plastic strain of three specimens under different impact energies.

observed for strain rates below 10^{-6} s^{-1}, and a change in slope occurs at a strain rate of 1.0 s^{-1} [48]. The following presents the DIF of cementitious materials in tension at high strain rates based on existing literature. At the experimental strain rate of 157 s^{-1}, concrete in tension exhibited a dynamic increase factor (DIF) of approximately 7.0 [48]. The SHCC experiments demonstrated a significant strain rate effect on tensile strength, resulting in a DIF of 6.7 when the measured strain rates ranged from 140 s^{-1} to 180 s^{-1} [49]. The increase in tensile strength of SHCC resembles the strain rate effect noted in equivalent tests on conventional and high-performance concretes. The DIF of tensile strength reached 6.0 for conventional concrete, while ranging from 3.8 for high-performance concrete (HPC) to 5.3 for ultra-high-performance concrete (UHPC) with fibers when the strain rate is about 100 s^{-1} [50]. The DIF for the tensile strength of plain geopolymers (GP) matrix equals 6.5 measured by a gravity-driven split-Hopkinson tension bar (SHTB) at strain rates of up to 300 s^{-1} [51]. Additional data from existing literature and the *fib* standard is provided in Appendix D. With a side length of 20 mm, the unit cell of ACCCs specimens in this study has a ligament of 2.0 mm, upon which the hammer tip impacts at a velocity of 1582.8 mm/s. Given this high strain rate, the model in this study adopted a DIF of 8.5, determined through comparing simulation results with experimental data. The strain rate sensitivity of the elastic modulus showed a much smaller effect [52,53]. In the case of SHCC, its elastic modulus exhibited a corresponding DIF of only 1.2 [49], whereas other concretes displayed lower DIF values or no increase in elastic modulus [50]. Therefore, the effect of strain rate on the elastic modulus was not considered in this model.

3.2. Modelling results and discussion

As shown in Fig. 17a, the simulated results have a good agreement with the experimental data regarding the energy absorption of the three specimens for the initial impact, thereby validating our model. In the experiments, the energy absorption of specimens P0, P25, and P50

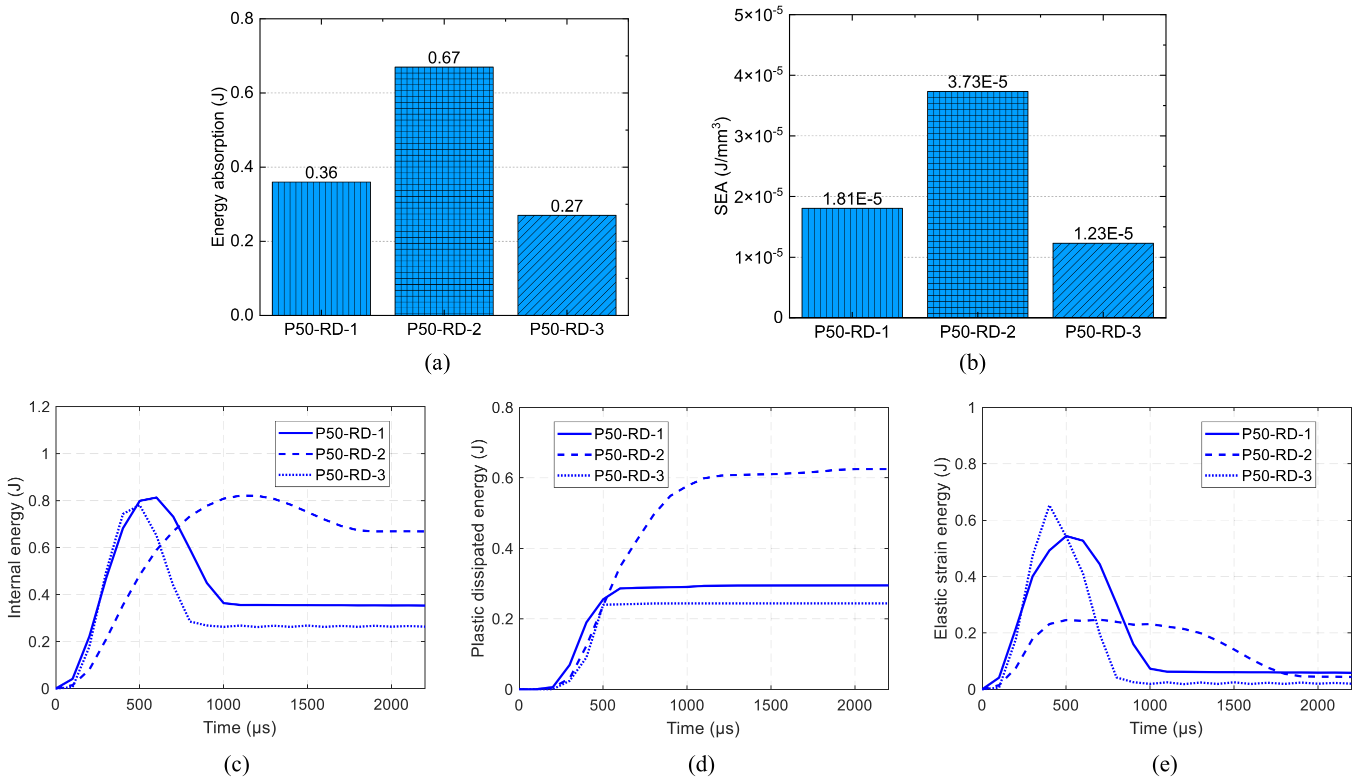

Fig. 23. Energy absorption (a), SEA (b), internal energy (c), plastic dissipation energy (d) and elastic strain energy (e) of P50 for different relative densities.

Table 7
Hammer velocities for different impact energies.

Label	IE-1 (1.0x)	IE-2 (2.0x)	IE-3 (3.0x)	IE-4 (4.0x)
Impact energy (J)	0.833	1.666	2.499	3.332
Velocity (mm/s)	1582.8	2238.4	2741.5	3165.6

during the initial impact is 0.541,0.407,0.337, respectively. In the model, the energy absorption of specimens P0, P25, and P50 during the initial impact is 0.550, 0.495, 0.356, respectively.

Fig. 17b shows the internal energy variation of the three specimens during the initial impact in the model. In Eq. (5), when the artificial strain energy is negligible, the internal energy of a specimen in the model can primarily be considered as the sum of the plastic dissipated energy (Fig. 17c) and the elastic strain energy (Fig. 17d). Upon contact with the impact hammer, the three specimens experience a rapid increase in elastic strain energy, while the plastic dissipated energy appears slightly later but also begins to rise. As a result, the hammer's kinetic energy decreases as it transfers energy to the internal energy of the specimens, as illustrated in Fig. 17e. Compared to P0, P25 and P50 show a quicker increase in elastic strain energy and a more delayed onset of plastic dissipated energy following impact. The internal energy of the specimens peaks when the hammer's kinetic energy is fully transferred and reduced to zero, causing both elastic strain energy and plastic dissipated energy to reach their maximum values. The elastic strain energy is then transferred back to the hammer, which is achieve by a reactive contact force and the resulting acceleration applied on the hammer. As a result, the specimens' internal energy decreases. This process ultimately causes the hammer to gradually disengage and rebound with a reversed velocity. Finally, the internal energy of the specimens stabilizes as the hammer disengages and its kinetic energy becomes constant, with plastic dissipated energy and a smaller amount of elastic strain energy remaining. It should be noted that P25 and P50 stabilize at a lower level of plastic dissipated energy absorption compared to P0. Specifically, P50 shows a slower rate of dissipated

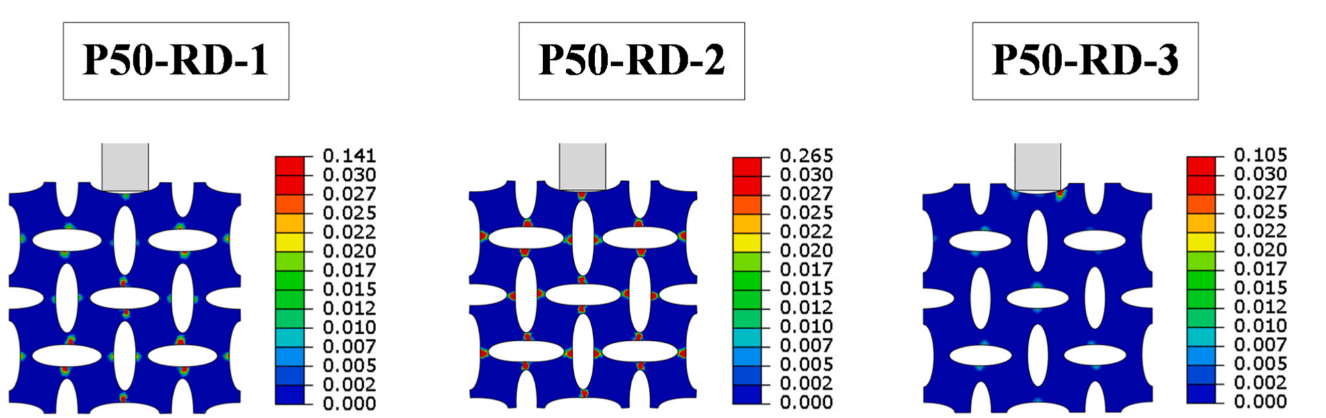

Fig. 24. Maximum principal plastic strain of P50 for different relative densities.

Table 8
Energy absorption of specimens under different impact energies.

Label	IE-1 (1.0x)	IE-2 (2.0x)	IE-3 (3.0x)	IE-4 (4.0x)
Impact energy (J)	0.833	1.666	2.499	3.332
Energy Absorption (P0)	0.550 (66.0 %)	1.600 (96.0 %)	2.203 (88.2 %)	2.755 (82.7 %)
Energy Absorption (P25)	0.494 (59.3 %)	0.972 (58.3 %)	1.828 (73.1 %)	2.387 (71.6 %)
Energy Absorption (P50)	0.355 (42.6 %)	1.217 (73.0 %)	2.073 (83.0 %)	2.968 (89.1 %)

energy absorption and reaches a lower stabilization point than P25. As shown in Fig. 17f, the total energy from the impact remains constant in the model during the initial impact. Figs. 18–20 display the maximum principal plastic strain of the three specimens after the initial impact in the model, which serves as an indicator to evaluate the crack-induced damage in cementitious materials. This helps elucidate the difference observed in the energy absorption process among the three specimens depicted in Fig. 17. The time shown in Figs. 18–20 represents the duration from the moment the hammer impacts the specimen to the point where the internal energy stabilizes after the hammer disengages and rebounds. To improve the visualization of the plastic strain distribution in Figs. 18–20, a threshold of 0.03 strain was applied, with strains exceeding this value being indicated in red.

As depicted in Fig. 18, P0 experiences a significant initial plastic strain exceeding 0.03 within 200μs upon impact from the hammer, localized solely in the impact zone. Conversely, ACCCs specimens show minor plastic strain at the same time interval, maintaining the majority of their structure's elasticity. It's noteworthy that P50 exhibits only minimal plastic strain in the lower part of its structure near the bottom plate, indicating its great ability to transfer impact energy to other structural parts through auxetic behavior. Conversely, P25 disperses its plastic strain within the vicinity of the impacted region of the structure. As the hammer tip gradually penetrates from 200μs to 1000μs, P0 undergoes increased localized damage within the impact zone, propagating the impact force downward along the direction of impact and resulting in the formation of a second major plastic damage at the lower ligament. Hence, significant localized damage occurs in the impact zone, resulting in a maximum plastic strain of 0.736. In contrast, within the same duration of impact hammer penetration, ACCCs specimens continue to disperse the impact energy to other parts of the specimen through auxetic behavior, thus reducing local damage. P25 remains limited to dispersing the impact energy to the upper half of the structure where the impact zone is located, reducing the maximum structural plastic strain to 0.678. However, the enhanced auxetic behavior of P50 resulting from its greater aspect ratio facilitates the rotation of a substantial portion of its ligaments throughout its entire structure. This disperses the impact energy and minimizes the maximum plastic strain to a minimum value of 0.141. This is attributed to the increase of the major axis in the P50 specimen (i.e., greater aspect ratio), which increases the horizontal distance between the vertical forces transmitted through the ligaments. Consequently, this generates a larger bending moment, causing more ligaments to undergo plastic damage and resulting in the rotation of the section. For the initial impact, the major plastic strain distributions of the three specimens in Figs. 18–20 closely resemble those observed in the DIC results. Similarly to the DIC results, the variations in plastic strain distribution among the three specimens in the model remain relatively minor after 500μs or 600μs for the initial impact.(Figs. 21–23)

3.3. Parametric analysis

3.3.1. Effect of impact energy

For the Schmidt hammer OS-120PM used in experiments, each single impact delivers 0.833 J of kinetic energy to the surface of the tested specimen via the impact tip. This section studies the effects of different impact energies on the impact resistance of ACCCs specimens. The corresponding velocity of the hammer in the model for each impact energy was given in Table 7. Fig. 21 shows internal, plastic dissipated, and elastic strain energy of three specimens under different impact energies. Fig. 22 displays the distribution of the maximum principal plastic strain for the three specimens after the internal energy has stabilized under different impact energies. As with previous figures, the color bars in Fig. 22 represent the maximum principal plastic strain. To improve the visualization of the plastic strain distribution in Fig. 22 (and similarly in Figs. 24, 26, 28), a threshold of 0.03 strain was applied, with strains exceeding this value being indicated in red. Table 8 presents the absorption energy of the specimens at different impact energies, with the percentages representing the ratio of absorbed energy to the total impact energy for each case.

As the impact energy increases, the internal energy of the three specimens rises significantly in Fig. 21. Specifically, their plastic dissipated energy increases markedly, whereas their elastic strain energy shows only a slight rise. As shown in Fig. 22, under IE-2 impact energy, the P0 specimen exhibits significant localized plastic damage with a maximum plastic strain of 1.815 in the impact zone, indicating large

Table 9
Different relative densities for P50.

Label	Major axis (mm)	Minor axis (mm)	Aspect ratio	Ellipse area (mm^2)	Specimen side length (mm)	Specimen thickness (mm)	Specimen volume (cm^3)	Relative density
P50-RD−1 (1.0x)	12.00	4.00	3	37.70	40	20	19.94	62.30 %
P50-RD−2 (0.9x)	12.95	4.32	3	43.93	40	20	17.94	56.07 %
P50-RD−3 (1.1x)	10.96	3.65	3	31.47	40	20	21.93	68.53 %

Table 10
Different specimen sizes for P50.

Label	Major axis (mm)	Minor axis (mm)	Aspect ratio	One Ellipse area (mm^2)	Specimen side length (mm)	Specimen thickness (mm)	Specimen volume (cm^3)	Relative density
P50-Size−1 (1.0x)	12	4	3	37.7	40	20	19.9	62.30 %
P50-Size−2 (1.5x)	18	6	3	84.8	60	20	44.9	62.30 %
P50-Size−3 (2.0x)	24	8	3	150.8	80	20	79.7	62.30 %

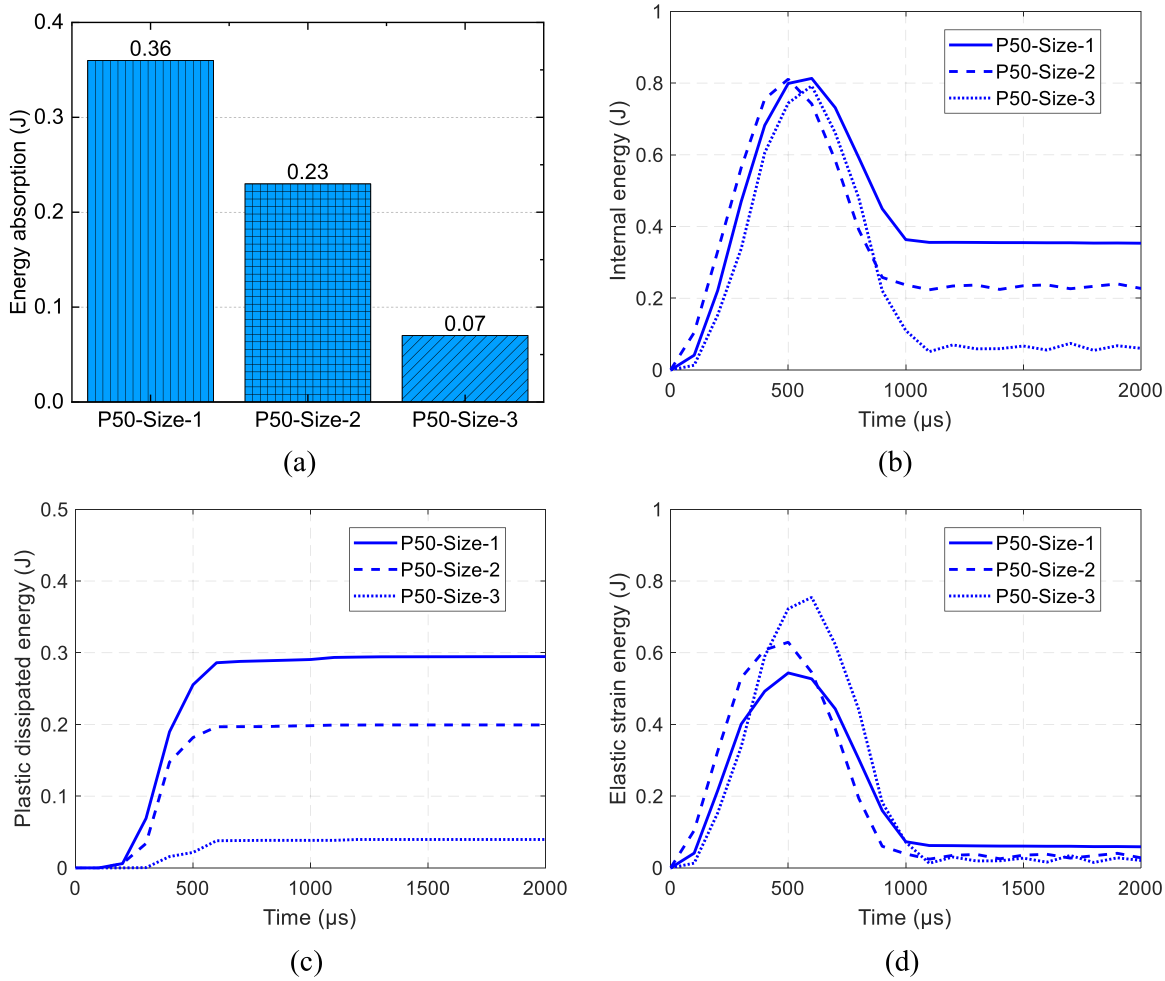

Fig. 25. Energy absorption (a), internal energy (b), plastic dissipation energy (c), and elastic strain energy (d) of P50 for different specimen sizes.

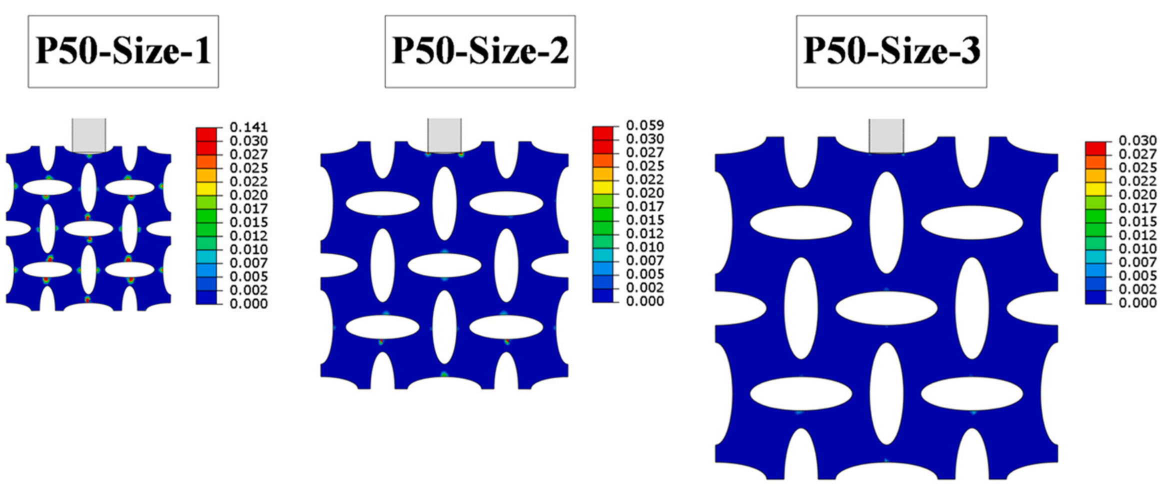

Fig. 26. Maximum principal plastic strain of P50 for different specimen sizes.

cracks and material failure. This propagates the impact force downward along the direction of impact, leading to substantial damage in the lower ligaments and structural splitting along the middle of the specimen. In Fig. 21, the plastic dissipated energy of P0 increases significantly under IE-2 due to intensified localized damage and the formation of midsection cracks. At IE-3 and IE-4 impact energies, localized damage and structural splitting become more severe (Fig. 22), with localized plastic strain increasing to 2.462 and 2.690 in the impact zone, respectively. This restricts the contribution of other structural parts to load-bearing and resulting in a limited increase in plastic dissipated energy in Fig. 21.

Conversely, ACCCs specimens mitigate the localized damage and structural splitting through auxetic behavior. Under IE-2 impact energy, the upper half of the P25 structure contracts and redistributes impact energy to other parts, thereby limiting further increase in localized

Table 11
Different RVEs for P50.

Label	Major axis (mm)	Minor axis (mm)	Aspect ratio	One Ellipse area (mm^2)	Specimen side length (mm)	Specimen thickness (mm)	Specimen volume (cm^3)	Relative density
2×2	12	4	3	37.7	40	20	19.9	62.30 %
4 × 4	12	4	3	37.7	80	20	79.6	62.30 %
8 × 8	12	4	3	37.7	160	20	318.4	62.30 %
16 × 16	12	4	3	37.7	320	20	1273.6	62.30 %

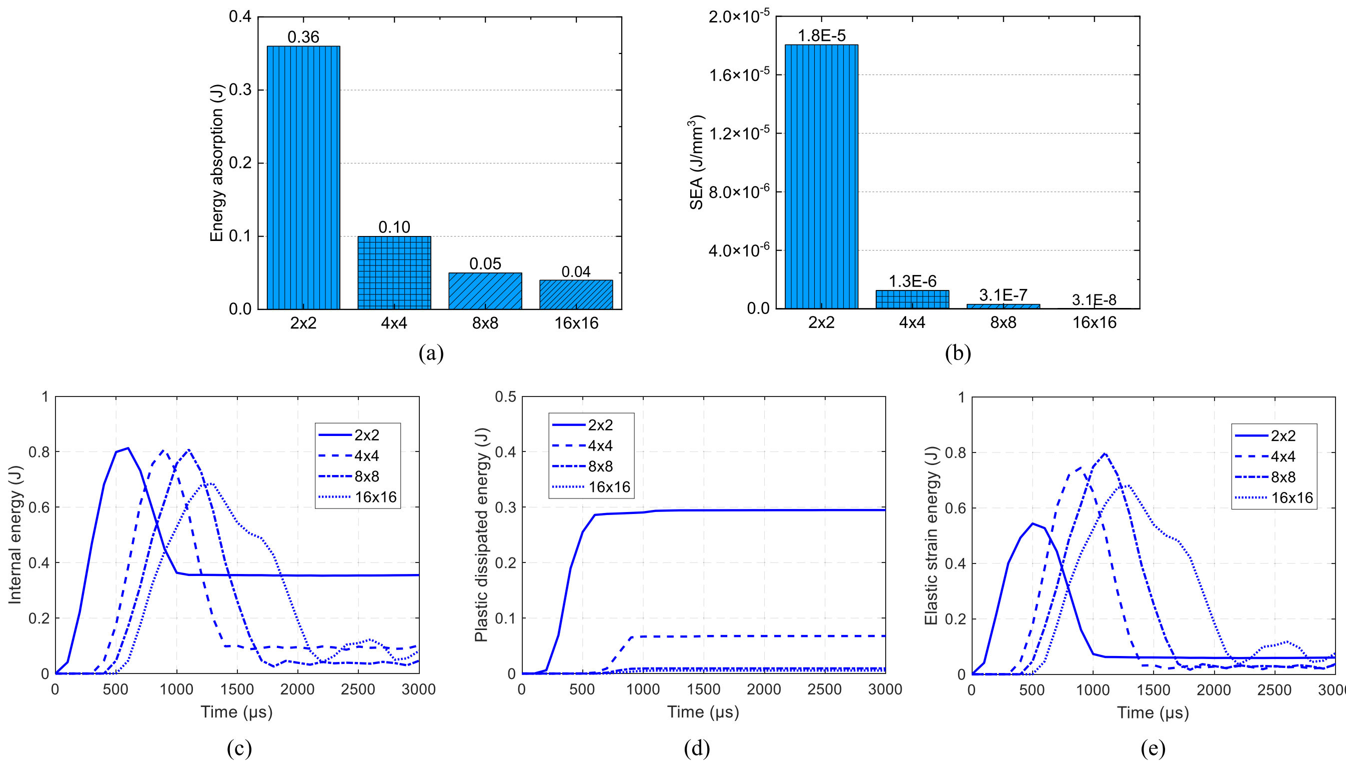

Fig. 27. Energy absorption (a), SEA (b), internal energy (c), plastic dissipation energy (d), and elastic strain energy (e) of P50 for different RVE sizes.

damage in the impact zone compared to IE-1 impact energy, as show in Fig. 22. However, P25's ability to disperse impact energy through auxetic behavior is mainly confined to the upper half of the structure. At higher impact energies of IE-3 and IE-4, localized damage intensifies, with maximum plastic strains rising to 1.458 and 1.448, respectively. This results in the expansion of the upper half of the structure and a tendency for splitting along the specimen's midsection, causing a significant increase in the plastic dissipated energy of P25 between IE-2 and IE-3 impact energies, as shown in Fig. 21. The potential structural splitting also restricts the further force transfer in P25, which shows a limited increase of plastic dissipated energy from IE-3 to IE-4. Under IE-2 impact energy, P50's enhanced auxetic behavior facilitates plastic deformation through ligament rotation across the entire structure, pulling more material into the impact zone and dispersing energy, as shown in Fig. 22. This results in a significant increase in plastic dissipated energy from IE-1 to IE-2 (Fig. 21), while keeping the maximum plastic strain slightly elevated at 0.295, thereby significantly reducing localized damage. Even at higher impact energies (IE-3 and IE-4), the continued ligament rotation aids in uniform plastic deformation and energy dissipation throughout the structure, leading to a steady increase in plastic dissipated energy. This helps keep the maximum plastic strain below 1.0, limiting localized damage and preserving structural integrity.

3.3.2. Effect of relative density

This section examines the impact of relative density on the impact resistance of ACCCs specimens, as detailed in Table 9. Relative density is a dimensionless measure that quantifies the ratio of the material's volume to the volume of the smallest enclosing cuboid, and it also indirectly reflects the influence of the elliptical hole area when the specimen thickness remains constant. The focus is on P50 specimen (P50-RD-1) studied above with a specific aspect ratio and specimen size, exploring changes when their relative density is scaled by 0.9x (P50-RD-2) and 1.1x (P50-RD-3). To maintain auxetic behavior for the P50 shape, the relative density scaling factor is kept relatively small. Fig. 23 illustrates the energy absorption, internal energy, plastic dissipation, and elastic strain energy of P50 for different relative densities. Fig. 24 shows the distribution of maximum principal plastic strain for P50 at various relative densities after internal energy has stabilized, with color bars representing the strain levels.

As shown in Fig. 23, energy absorption, SEA and stabilized internal energy decrease as P50 relative density increases. Concurrently, plastic dissipated energy decreases while elastic strain energy increases with higher relative density. Specifically, P50-RD-2 with the lowest relative density shows a notable rise in plastic dissipated energy and a decrease in elastic strain energy, attributed to reduced joint size leading to greater plastic deformation during section rotation. Despite this, Fig. 24 shows that the plastic strain does not increase significantly, and localized damage in the impact zone remains limited, maintaining overall structural integrity. In contrast, when the relative density is increased to 1.1 times (P50-RD-3), plastic strain drops to a minimal value of 0.105, with most of the specimen retaining its elastic properties.

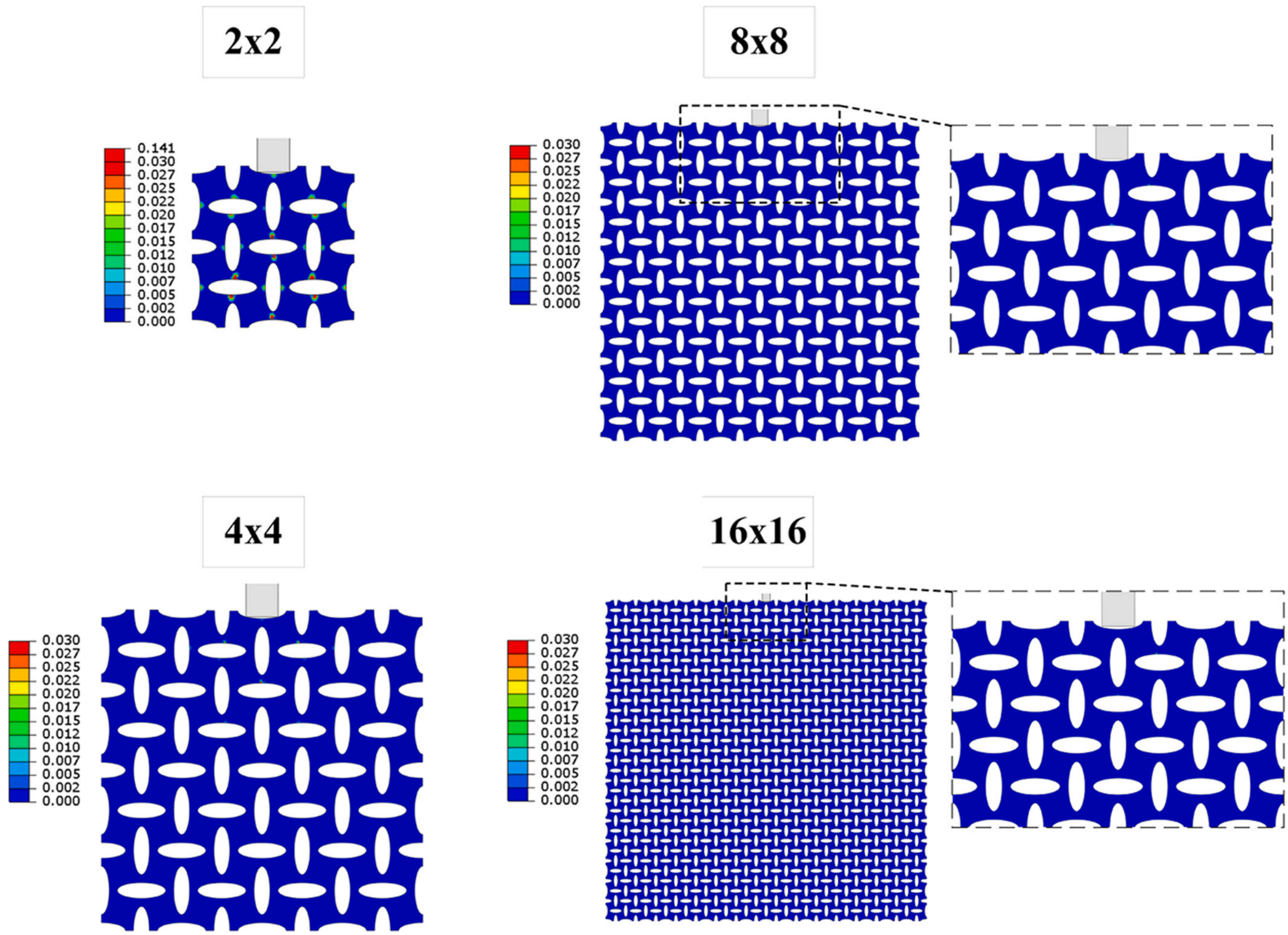

Fig. 28. Maximum principal plastic strain of P50 for different RVE sizes.

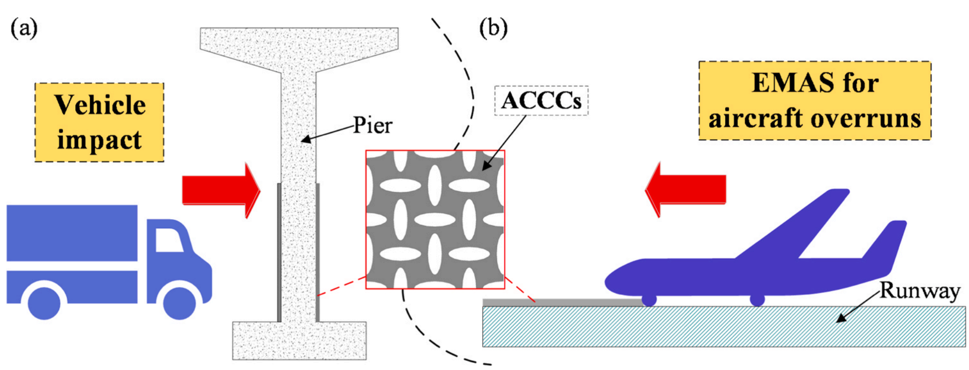

Fig. 29. Potential engineering applications of ACCCs for impact mitigation, (a) sacrificial protective materials in bridge piers, (b) EMAS with high energy absorption.

3.3.3. Effect of specimen size

This section examines the impact resistance of ACCCs specimens across different sizes, as listed in Table 10. The section focuses on the P50 specimen (P50-Size-1) studied above with a specific aspect ratio and relative density, examining changes when the specimen size is scaled by 1.5x (P50-Size-2) and 2x (P50-Size-3). Fig. 25 shows the energy absorption, internal energy, plastic dissipation, and elastic strain energy of P50 for various specimen sizes. Fig. 26 displays the distribution of maximum principal plastic strain for P50 with various specimen sizes after internal energy stabilization, with color bars indicating the strain levels. As seen in Fig. 25, both energy absorption and stabilized internal energy decrease with increasing P50 specimen size. Correspondingly, plastic dissipated energy decreases, while elastic strain energy increases as the specimen size increases. Fig. 26 shows a marked reduction in plastic strain with larger specimen sizes. Specifically, when the specimen size is increased to 2.0 times (P50-size-3), the plastic strain falls to a minimal value of 0.014, and the majority of the specimen maintains its elastic properties.

3.3.4. Effect of representative volume element (RVE) size

This section explores the impact resistance of ACCCs specimens across different RVE sizes, while keeping the unit cell dimensions constant, as listed in Table 11. The analysis focuses on the P50 specimen (2×2) studied previously with a specific aspect ratio and relative density, and investigates how the impact resistance changes when the RVE size is changed to 4 × 4, 8×8, and 16x16. Fig. 27 presents data on energy absorption, internal energy, plastic dissipation, and elastic strain energy for P50 across these RVE sizes. Fig. 28 illustrates their distribution of maximum principal plastic strain after internal energy stabilization, with color bars indicating strain levels. As shown in Fig. 27, both energy absorption and SEA decrease as the RVE size increases. The stabilized internal energy and plastic dissipation decrease, while elastic strain energy increases when the RVE size grows from 2×2 to 8×8. When the RVE size further increases to 16x16, the plastic dissipation remains almost unchanged, but internal and elastic strain energy extend and fluctuate after the tip detaches from the specimen. Fig. 28 reveals a significant reduction in plastic strain with larger RVE size. Specifically, when the RVE size is increased to 16x16, the plastic strain drops to a minimal value of 0.01, with most of the specimen maintaining its elastic properties.

4. Conclusions

In this study, ACCCs with different aspect ratios, designated as P25 and P50, were manufactured to analyze their impact response, while specimen P0 with circular holes was included for comparison. Additionally, a numerical model was established to simulate the impact behavior of the specimens, followed by parametric analysis to gain further insights. The main conclusions are as follows:

(1) ACCC specimens exhibit significant major strain dispersion along the ligaments throughout a substantial portion of the structure due to auxetic behavior. This results in the involvement of surrounding material into the impact zone, enhancing the efficient transfer of impact energy across the structure to strengthen contact stiffness and mitigate localized damage in the impact zone, thereby maintaining overall structural integrity. Conversely, major strain in P0 specimens is only concentrated in the middle ligaments near the impact zone.

(2) Compared to the reference (P0), ACCCs specimens experience less localized damage in the impact zone during the initial impact due to their auxetic behavior. This leads to higher peak reaction forces and greater elastic strain energy per impact. Over successive impacts, ACCCs specimens accumulate local damage more slowly, allowing them to maintain higher peak reaction forces and endure more impacts until failure. Consequently, they achieve greater total energy absorption until failure. Specifically, P50 exhibits higher impact resistance than P25 due to the enhanced auxetic behavior resulting from its greater aspect ratio. This creates a greater bending moment to enable more ligaments to dissipate energy through rotation-induced plastic deformation, thereby reducing localized damage.

(3) Parametric analysis reveals that as impact energy increases, localized damage in the impact zone and structural splitting become more severe for P0 specimens. In contrast, ACCC specimens achieve higher energy absorption through plastic dissipation in ligaments triggered by auxetic behavior, which helps to mitigate the localized damage and maintain structural integrity. For the P50 pattern, localized damage decreases with increasing relative density and also reduces as the specimen size and RVE size increase. Even at lower relative densities, the energy absorption from plastic dissipation of ligaments remains high, yet the localized damage does not increase significantly and overall structural integrity is maintained.

This study shows that ACCCs specimens with a higher water-cement ratio exhibit increased fluidity for smooth casting and improved ductility in fiber-reinforced concrete. This allows cracks to act as hinge points to achieve auxetic behavior under compression. However, the weaker material strength of P25 leads to some localized damage under impact, reducing its auxetic behavior. Conversely, P50, despite its lower material strength, can enhance local impact resistance due to its greater auxetic behavior. Future adjustments in mixture proportions or the use of SHCC could further enhance material strength and reduce damage, particularly improving impact resistance in P25. Moreover, future research will explore the out-of-plane impact behavior of 3D auxetic cementitious materials to broaden their engineering applications. However, fabricating 3D auxetic cementitious materials using a fiber-reinforced matrix poses significant challenges, which will also be addressed in subsequent studies. Based on this study, ACCCs specimens demonstrate significant impact resistance, enhanced energy absorption and localized stiffness upon impact, and high endurance under multiple impacts. Considering the widespread availability of cementitious materials, lightweight and high energy-absorbing ACCCs can be used as sacrificial protective materials in infrastructure (such as building walls, columns, and bridge piers (Fig. 29a)) to dissipate impact energy and mitigate localized damage. Additionally, the proposed ACCCs can be used to develop next-generation shock-absorbing engineered materials arresting system (EMAS) [54,55]. These high-energy absorbing strips are placed at runway ends to reduce the impact of aircraft overruns (Fig. 29b).

CRediT authorship contribution statement

Jinbao Xie: Writing – original draft, Writing – review & editing, Validation, Software, Methodology, Formal analysis, Data curation, Conceptualization. **Yading Xu:** Writing – review & editing, Methodology, Formal analysis, Conceptualization. **Zhaozheng Meng:** Writing – review & editing, Software. **Minfei Liang:** Writing – review & editing, Visualization. **Yubao Zhou:** Writing – review & editing, Validation. **Branko Šavija:** Writing – review & editing, Validation, Supervision, Resources, Methodology, Funding acquisition, Conceptualization, Project administration.

Declaration of Competing Interest

The authors declare that they have no known competing financial interests or personal relationships that could have appeared to influence the work reported in this paper.

Acknowledgements

Jinbao Xie, Minfei Liang, Yubao Zhou would like to acknowledge the funding supported by China Scholarship Council (CSC) under the grant CSC No. 202006260045, 202007000027, 202006260051. Yading Xu, Zhaozheng Meng, Branko Šavija acknowledge the financial support of the European Research Council (ERC) within the framework of the ERC Starting Grant Project “Auxetic Cementitious Composites by 3D printing (ACC-3D)”, Grant Agreement Number 101041342. Views and opinions expressed are however those of the author(s) only and do not necessarily reflect those of the European Union or the European Research Council. Neither the European Union nor the granting authority can be held responsible for them.

Appendix A

Quasi-static tests results of specimens P0, P25, P50

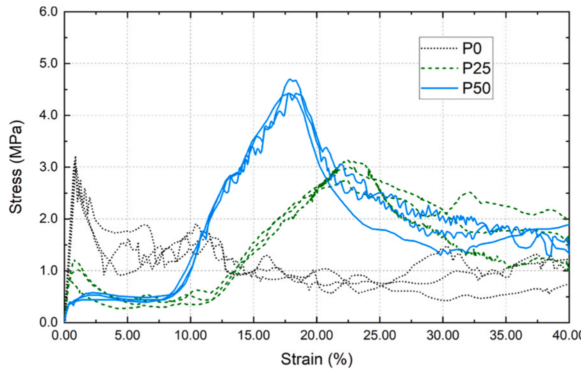

Fig. A1. Stress–strain curves of specimens P0, P25, P50 under uniaxial compression tests until 40 % strain [41]

Appendix B

A concise overview of Concrete Damage Plasticity (CDP) model

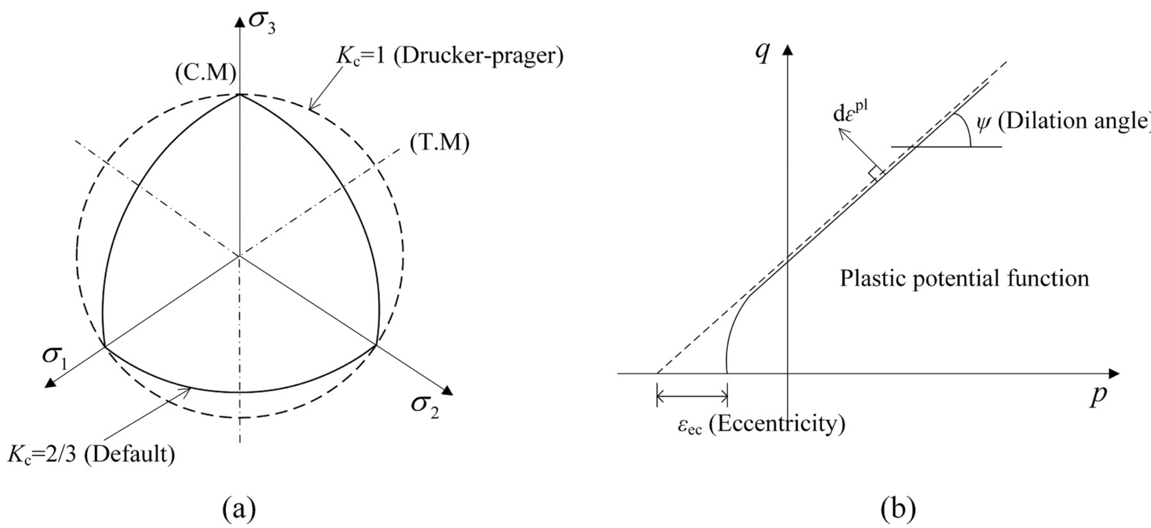

Fig. B1. Yield surface and flow rule of CDP model, (a) yield surface in the deviatoric plane, (b) dilation angle and eccentricity in meridian plane

In this study, the Concrete Damage Plasticity (CDP) model [34,56–61] was utilized to simulate the nonlinear behavior of cementitious materials, accounting for both plasticity and damage effects.

$$\sigma = (1-d)D_0^{el} : (\varepsilon - \varepsilon^{pl}) \tag{B1}$$

$$\varepsilon = \varepsilon^{el} + \varepsilon^{pl} \tag{B2}$$

$$\overline{\sigma} = \frac{\sigma}{1-d} \tag{B3}$$

where σ is the stress; $\overline{\sigma}$ is the effective stress; $\varepsilon, \varepsilon^{el}, \varepsilon^{pl}$ are the total strain, elastic strain, and plastic strain, respectively. D_0^{el} represents the initial, undamaged stiffness of cementitious material. d represents the damage factor used to quantify stiffness degradation, ranging from 0 to 1. It is required that d increases monotonically with plastic strain. However, since fiber-reinforced cementitious material was utilized, stress does not decrease monotonically with the increase of plastic strain when the material is subjected to tension. Therefore, d could not be considered. In this study, plastic strain serves as a measurable indicator for assessing crack-induced damage in cementitious materials.

The following yield criterion in the CDP model is used to characterize the initiation of plastic strain.

$$F = \frac{1}{1-\alpha}\left(\overline{q} - 3\alpha\overline{p} + \beta\left(\varepsilon^{pl}\right)\langle\widehat{\overline{\sigma}}_{\max}\rangle - \gamma\langle-\widehat{\overline{\sigma}}_{\max}\rangle\right) - \widehat{\overline{\sigma}}_c\left(\varepsilon_c^{pl}\right) \tag{B4}$$

Where

$$\overline{p} = -\frac{1}{3}trace(\overline{\sigma}) \tag{B5}$$

$$\overline{q} = \sqrt{\frac{3}{2}(\overline{S}:\overline{S})} \tag{B6}$$

$$\overline{S} = \overline{\sigma} + \overline{p}I \tag{B7}$$

$$\alpha = \frac{(\sigma_{b0}/\sigma_{c0}) - 1}{2\cdot(\sigma_{b0}/\sigma_{c0}) - 1} \tag{B8}$$

$$\beta = \frac{\overline{\sigma_c}(\varepsilon_c^{pl})}{\overline{\sigma_t}(\varepsilon_t^{pl}) - 1}(1-\alpha) - (1+\alpha) \tag{B9}$$

$$\gamma = \frac{3\cdot(1-K_c)}{2\cdot K_c - 1} \tag{B10}$$

where $\overline{p}$ and $\overline{q}$, as the two stress invariants of the effective stress, represent the hydrostatic pressure stress and the von Mises equivalent effective stress. $\overline{S}$ is the effective stress deviator. I is the unit tensor. The subscripts t and c denote the values for tension and compression, respectively. $\widehat{\overline{\sigma}}_{\max}$ is the maximum principal effective stress. σ_{b0}/σ_{c0} refers to the ratio of equi-biaxial and uniaxial compressive yield stress, which is usually assumed as 1.16 in ABAQUS. K_c describes the ratio of the second stress invariant on the tensile meridian (T.M) to that on the compressive meridian (C.M) for a given invariant $\overline{p}$, which has a default value of 0.667 in ABAQUS. K_c defines the shape of the yield surface on the deviatoric plane, as shown in Fig. B1a.

The CDP model assumes non-associated potential plastic flow. The flow potential $G(\sigma)$, derived from the Drucker-Prager hyperbolic function, is defined as

$$G(\sigma) = \sqrt{(\varepsilon_{ec}\sigma_{t0}\tan\psi)^2 + \overline{q}^2} - \overline{p}\tan\psi \tag{B11}$$

where ψ is the dilation angle measured in the $\overline{p} - \overline{q}$ plane at high confining pressure. ε_{ec} is the eccentricity that determines the rate at which the function approaches the asymptote (see Fig. B1b) and typically has a value of 0.1 in ABAQUS. σ_{t0} is the uniaxial tensile stress at failure.

Appendix C

HJC (Holmquist-Johnson-Cook) model

The HJC (Holmquist-Johnson-Cook) model is a constitutive model developed to characterize the dynamic response of brittle materials like concrete, rocks, and ceramics under conditions of high strain rates, high pressures, and significant deformations [62,63]. In literature [64], the HJC model was used to simulate the dynamic behavior of brittle aggergate in concrete under impact loading. However, fiber-reinforced cementitious materials exhibit significantly greater ductility, and thus, further investigation is needed to determine if the HJC model can be directly applied to these materials. The HJC model mainly includes three parts: the equation of yield surface, equation of damage evolution, and equation of state. Yet the use of the HJC model is significantly limited due to the requirement of determining its 27 parameters, which are obtained under complex experimental conditions. Specifically, the parameters of B, N in the equation of yield surface (Eq. C1) need to be determined from the triaxial test of the material. The strain rate constant C in the equation of yield surface (Eq. C1) can be determined by the SHPB test of specimens. The three parameters of are $D1$, $D2$ and *EFMIN* in the equation of damage evolution (Eq. C2) need to be determined from the uniaxial loading test of specimens. P_{lock}, K_1, K_2 and K_3 in the equation of state (Eq. C3) need to be determined by the Hugoniot test. Moreover, the HJC model neglects the tensile damage criteria and cannot capture the tensile failure of materials. Additionally, the third deviatoric stress invariant J3 is also omitted in the HJC model.

The equation of yield surface is given as

$$\sigma^* = \left[A(1-D) + BP^{*N}\right](1 + C\ln\dot{\varepsilon}^*) \leq S_{\max} \tag{C1}$$

where $\sigma^* = \sigma/f'_c$ and $P^* = P/f'_c$ are the normalized equivalent stress and hydrostatic pressure, respectively. f'_c is the compressive strength. σ is the actual equivalent stress. P refers to the actual pressure. A refers to the normalized cohesive strength. $\dot{\varepsilon}^* = \dot{\varepsilon}/\dot{\varepsilon}_0$ represents the dimensionless strain rate, where $\dot{\varepsilon}$ and $\dot{\varepsilon}_0 = 1.0s^{-1}$ are the actual and reference strain rates, respectively. D is the damage factor, ranging from 0 to 1. C refers to the strain rate constant. B is the normalized pressure hardening coefficient. N represents the pressure hardening exponent. S_{max} is the normalized maximum strength.

The equation of damage is expressed as

$$D = \sum\frac{\Delta\varepsilon_P + \Delta\mu_P}{\varepsilon_P^f + \mu_P^f} = \sum\frac{\Delta\varepsilon_P + \Delta\mu_P}{D_1(P^* + T^*)^{D_2}} \geq EFMIN \tag{C2}$$

where $\Delta\varepsilon_P$ and $\Delta\mu_P$ represent the equivalent plastic strain and the plastic volumetric strain, respectively, during an integration cycle. $\varepsilon_P^f + \mu_P^f$ refers to the plastic strain up to fracture under constant pressure P. $T^* = T/f'_c$ is the normalized maximum tensile hydrostatic pressure, where T is the maximum tensile hydrostatic pressure that the material can endure. D_1 and D_2 are damage constants. *EFMIN* is a material constant used to suppress fracture from weak tensile waves.

The equation of state is

$$P = \begin{cases} K_{elastic}\mu, P \le P_{crush} \\ \dfrac{P_{crush} - P_{lock}}{\mu_{crush} - \mu_{lock}}(\mu - \mu_{crush}) + P_{crush}, P_{crush} < P < P_{lock} \\ K_1\overline{\mu} + K_2\overline{\mu}^2 + K_3\overline{\mu}^3, P \ge P_{lock} \end{cases} \tag{C3}$$

where $\mu = \rho/\rho_0 - 1$ is the volumetric strain, where ρ and ρ_0 are the current density and initial density, respectively. $K_{elastic} = P_{crush}/\mu_{crush}$ refers to the elastic bulk modulus, where P_{crush} and μ_{crush} are the pressure and volumetric strain, respectively, when the material begins to undergo plastic deformation. μ_{plock} and $P_{lock}$are the volumetric strain and pressure, respectively, when the air voids are completely removed from the material. $\overline{\mu} = (\mu - \mu_{lock})/(1 + \mu_{lock})$ represents the modified volumetric strain. K_1, K_2 and K_3 are constants. μ_{lock} is the volumetric strain when the density ρ reaches the grain density ρ_{grain}.

Karagozian & Case (K&C) concrete (KCC) model

The KCC model was designed to analyze structures subjected to dynamic loadings, such as impacts and blasts. This model incorporates three pressure-sensitive, independent strength surfaces on the compressive meridian plane [65–67]: the maximum failure surface (Y_m), the initial failure surface (Y_i), and the residual failure surface (Y_r), as defined in Eq. (C4)–Eq. (C6). However, the eight parameters a_0, a_1, a_2, a_{0y}, a_{1y}, a_{2y}, a_{1f}, a_{2f} for the three surfaces need to be derived from triaxial tests of the material. Specially, a_{0f} in Eq. (C6) should be zero for concrete, as no residual strength is observed in uniaxial compression tests. But due to the fiber-bridging effect, ACCCs exhibit recoverable deformation after unloading, which requires further calibration of a_{0f} for ACCCs.

$$Y_m = \begin{cases} 3(P/\eta + f_t), P \le 0 \\ 1.5(P + f_t)/\psi(P), 0 < P \le f_c/3 \\ a_0 + P/(a_1 + a_2P), P > f_c/3 \end{cases} \tag{C4}$$

$$Y_i = \begin{cases} 1.35(P + f_t), P \le 0 \\ 1.35f_t + 3P\left(1 - 1.35f_t\big/f_{yc}\right), 0 < P \le f_{yc}\big/3 \\ a_{0y} + P\big/\left(a_{1y} + a_{2y}P\right), P > f_{yc}\big/3 \end{cases} \tag{C5}$$

$$Y_r = a_{0f} + P\big/(a_{1f} + a_{2f}P) \tag{C6}$$

where $\psi(P)$ denotes the ratio of the tensile to compressive meridian radii at a given pressure P. f_c is the uniaxial compressive strength. f_{yc} is initial yield compressive strength. f_t is the uniaxial tensile strength. η is the yield scale factor (0−1) that is related the accumulated equivalent plastic strain.

Moreover, it is important to note that $\psi(P)$ and the assumption $Y_i = 0.45Y_m$ may not be applicable to fiber-reinforced cementitious materials, as it is based on previous experimental data from normal concrete. Additionally, a notable drawback of this model is that the variation of fracture strain with strain rate is inconsistent with experimental observations [62].

ZWT model

The ZWT model is a nonlinear viscoelastic model to consider the dynamic constitutive behavior of polymers [68–71]. It is primarily used to describe the constitutive relationship of polymers within a strain rate range of 10^{-4} to 10^{-3}. Recently, the ZWT model has also been applied to studying the dynamic mechanical behavior of concrete-like materials. This model is particularly effective in capturing the dynamic response of materials exhibiting strain-hardening properties. However, it does not account for the damage characteristics that occur during deformation, limiting its ability to describe the dynamic mechanical behavior of concrete-like materials that exhibit distinct damage features and strain-softening behavior after reaching peak stress [69]. Additionally, the model's complexity, due to the large number of parameters, increases computational challenges.

Appendix D

The strain rate – DIF curve for concrete in compression according to the CEB-FIP model code 2010 (MC2010) [72–74] is

$$DIF = \begin{cases} \left(\dfrac{\dot{\varepsilon}}{\dot{\varepsilon}_c}\right)^{0.014} & if\ \ \dot{\varepsilon} \le 30s^{-1} \\ 0.012\left(\dfrac{\dot{\varepsilon}}{\dot{\varepsilon}_c}\right)^{1/3} & if\ \ \dot{\varepsilon} > 30s^{-1} \end{cases} \tag{D1}$$

Where $\dot{\varepsilon}_s = 30 \times 10^{-6}s^{-1}$ (quasi-static strain rate).

The strain rate – DIF curve for concrete in tension according to the CEB-FIP model code 2010 (MC2010) [72–74] is

$$DIF = \begin{cases} \left(\frac{\dot{\varepsilon}}{\dot{\varepsilon}_t}\right)^{0.018} & if \ \ \dot{\varepsilon} \le 10s^{-1} \\ 0.0062\left(\frac{\dot{\varepsilon}}{\dot{\varepsilon}_t}\right)^{1/3} & if \ \ \dot{\varepsilon} > 10s^{-1} \end{cases} \tag{D2}$$

Where $\dot{\varepsilon}_t = 10^{-6}s^{-1}$ (quasi-static strain rate).

The DIF values of cementitious materials in tension at high strain rates, obtained from existing literature [48–51,72,75,76] and the FIB standard (CEB-FIP Model Code 2010) [73], are presented below.

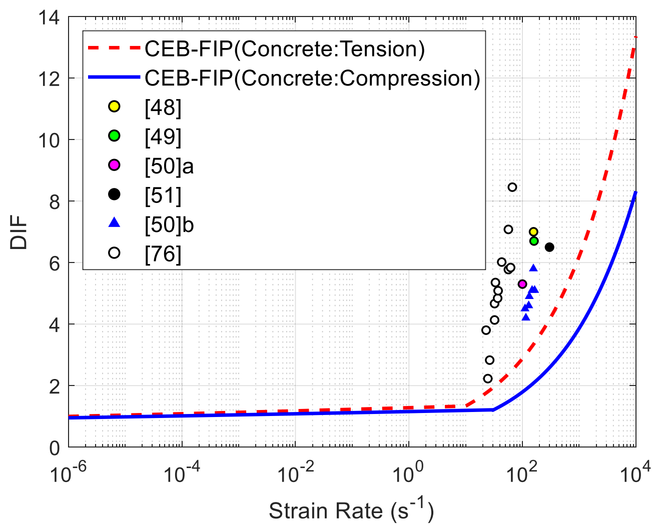

Fig. D1. DIF values of cementitious materials in tension at high strain rates from existing literature and *fib* standard (CEB-FIP model code 2010)

Data availability

Data will be made available on request.

References

[1] H. Jiang, J. Wang, G. Chorzepa, Mi, J. Zhao, Numerical investigation of progressive collapse of a multispan continuous bridge subjected to vessel collision, J. Bridge Eng. 22 (2017) 04017008, https://doi.org/10.1061/(ASCE)BE.1943-5592.0001037.
[2] W.J. Cantwell, J. Morton, The impact resistance of composite materials — a review, Composites 22 (1991) 347–362, https://doi.org/10.1016/0010-4361(91)90549-V.
[3] N. Ranwaha, S. Chung Kim Yuen, The effects of blast-induced fragments on cellular materials, Int. J. Impact Eng. 92 (2016) 50–65, https://doi.org/10.1016/j.ijimpeng.2015.12.003.
[4] R.P. Bohara, S. Linforth, T. Nguyen, A. Ghazlan, T. Ngo, Anti-blast and -impact performances of auxetic structures: a review of structures, materials, methods, and fabrications, Eng. Struct. 276 (2023) 115377, https://doi.org/10.1016/j.engstruct.2022.115377.
[5] K. Fujikake, B. Li, S. Soeun, Impact response of reinforced concrete beam and its analytical evaluation, J. Struct. Eng. 135 (2009) 938–950, https://doi.org/10.1061/(ASCE)ST.1943-541X.0000039.
[6] S. Şengel, H. Erol, T. Yılmaz, Ö. Anıl, Investigation of the effects of impactor geometry on impact behavior of reinforced concrete slabs, Eng. Struct. 263 (2022) 114429, https://doi.org/10.1016/j.engstruct.2022.114429.
[7] R. Yang, D. Qu, J. Zhang, G. Zhao, C. Gu, Numerical evaluation of impact resistance of reinforced concrete walls, Structures 64 (2024) 106518, https://doi.org/10.1016/j.istruc.2024.106518.
[8] H.C. Fu, M.A. Erki, M. Seckin, Review of Effects of Loading Rate on Reinforced Concrete, J. Struct. Eng. 117 (1991) 3660–3679, https://doi.org/10.1061/(ASCE)0733-9445(1991)117:12(3660).
[9] X. Bao, B. Li, Residual strength of blast damaged reinforced concrete columns, Int. J. Impact Eng. 37 (2010) 295–308, https://doi.org/10.1016/j.ijimpeng.2009.04.003.
[10] J. Ožbolt, A. Sharma, Numerical simulation of reinforced concrete beams with different shear reinforcements under dynamic impact loads, Int. J. Impact Eng. 38 (2011) 940–950, https://doi.org/10.1016/j.ijimpeng.2011.08.003.
[11] M.M. Kamran, M.A. Khan, Iqbal, An experimental investigation of plain, reinforced, and prestressed concrete slabs subjected to non-deformable projectile impact, Eng. Fail. Anal. 159 (2024) 108090, https://doi.org/10.1016/j.engfailanal.2024.108090.
[12] X. Luo, W. Sun, S.Y.N. Chan, Characteristics of high-performance steel fiber-reinforced concrete subject to high velocity impact, Cem. Concr. Res. 30 (2000) 907–914, https://doi.org/10.1016/S0008-8846(00)00255-6.
[13] J. Li, Y.X. Zhang, Chapter 14 - Numerical modeling of structural behavior of engineered cementitious composite (ECC) slabs subjected to high-velocity projectile impact, in: Y.X. Zhang, K. Yu (Eds.), Advances in Engineered Cementitious Composites, Woodhead Publishing, 2022, pp. 437–470.
[14] M.H. Zhang, M.S.H. Sharif, G. Lu, Impact resistance of high-strength fibre-reinforced concrete 59 (2007) 199–210, https://doi.org/10.1680/macr.2007.59.3.199.
[15] K.T. Soe, Y.X. Zhang, L.C. Zhang, Impact resistance of hybrid-fiber engineered cementitious composite panels, Compos. Struct. 104 (2013) 320–330, https://doi.org/10.1016/j.compstruct.2013.01.029.
[16] Y. Liu, Y. Wei, Drop-weight impact resistance of ultrahigh-performance concrete and the corresponding statistical analysis, J. Mater. Civ. Eng. 34 (2022) 04021409, https://doi.org/10.1061/(ASCE)MT.1943-5533.0004045.
[17] P.C. Jia, H. Wu, R. Wang, Q. Fang, Dynamic responses of reinforced ultra-high performance concrete members under low-velocity lateral impact, Int. J. Impact Eng. 150 (2021) 103818, https://doi.org/10.1016/j.ijimpeng.2021.103818.
[18] M. Chen, Z. Chen, Y. Xuan, T. Zhang, M. Zhang, Static and dynamic compressive behaviour of 3D printed auxetic lattice reinforced ultra-high performance concrete, Cem. Concr. Compos. 139 (2023) 105046, https://doi.org/10.1016/j.cemconcomp.2023.105046.
[19] K.E. Evans, M.A. Nkansah, I.J. Hutchinson, S.C. Rogers, Molecular network design, 124-124, Nature 353 (1991), https://doi.org/10.1038/353124a0.
[20] X. Xue, C. Lin, F. Wu, Z. Li, J. Liao, Lattice structures with negative Poisson's ratio: a review, Mater. Today Commun. 34 (2023) 105132, https://doi.org/10.1016/j.mtcomm.2022.105132.
[21] E.O. Momoh, A. Jayasinghe, M. Hajsadeghi, R. Vinai, K.E. Evans, P. Kripakaran, J. Orr, A state-of-the-art review on the application of auxetic materials in cementitious composites, Thin-Walled Struct. 196 (2024) 111447, https://doi.org/10.1016/j.tws.2023.111447.
[22] K.E. Evans, A. Alderson, Auxetic materials: functional materials and structures from lateral thinking!, Adv. Mater. 12 (2000) 617–628, https://doi.org/10.1002/(SICI)1521-4095(200005)12:9< 617::AID-ADMA617> 3.0.CO;2-3.

[23] Z.-Y. Li, W.-M. Zhang, S. Zou, X.-T. Wang, L. Ma, L.-Z. Wu, H. Hu, Quasi-static uniaxial compression and low-velocity impact properties of composite auxetic CorTube structure, Thin-Walled Struct. 202 (2024) 112059, https://doi.org/10.1016/j.tws.2024.112059.
[24] Z.-Y. Li, X.-T. Wang, L. Ma, L.-Z. Wu, Study on the mechanical properties of CFRP composite auxetic structures consist of corrugated sheets and tubes, Compos. Struct. 292 (2022) 115655, https://doi.org/10.1016/j.compstruct.2022.115655.
[25] Z.-Y. Li, X.-T. Wang, L. Ma, L.-Z. Wu, L. Wang, Auxetic and failure characteristics of composite stacked origami cellular materials under compression, Thin-Walled Struct. 184 (2023) 110453, https://doi.org/10.1016/j.tws.2022.110453.
[26] Z.-Y. Li, X.-T. Wang, J.-S. Yang, S. Li, K.-U. Schröder, Mechanical response and auxetic properties of composite double-arrow corrugated sandwich panels with defects, Mech. Adv. Mater. Struct. 29 (2022) 6517–6529, https://doi.org/10.1080/15376494.2021.1980926.
[27] G. Imbalzano, S. Linforth, T.D. Ngo, P.V.S. Lee, P. Tran, Blast resistance of auxetic and honeycomb sandwich panels: comparisons and parametric designs, Compos. Struct. 183 (2018) 242–261, https://doi.org/10.1016/j.compstruct.2017.03.018.
[28] Y. Luo, K. Yuan, L. Shen, J. Liu, Sandwich panel with in-plane honeycombs in different Poisson's ratio under low to medium impact loads 60 (2021) 145–157, https://doi.org/10.1515/rams-2021-0020.
[29] H. Yazdani Sarvestani, A.H. Akbarzadeh, H. Niknam, K. Hermenean, 3D printed architected polymeric sandwich panels: energy absorption and structural performance, Compos. Struct. 200 (2018) 886–909, https://doi.org/10.1016/j.compstruct.2018.04.002.
[30] C.W. Isaac, C. Ezekwem, A review of the crashworthiness performance of energy absorbing composite structure within the context of materials, manufacturing and maintenance for sustainability, Compos. Struct. 257 (2021) 113081, https://doi.org/10.1016/j.compstruct.2020.113081.
[31] Z.-Y. Li, J.-S. Yang, Z.-Y. Wang, H. Hu, H. Han, H.-Z. Li, J.-H. Wu, Static and dynamic study of fiber-reinforced hemispherical stacked sandwich structure, Compos. Struct. 329 (2024) 117809, https://doi.org/10.1016/j.compstruct.2023.117809.
[32] T. Gärtner, S.J. van den Boom, J. Weerheijm, L.J. Sluys, Geometric effects on impact mitigation in architected auxetic metamaterials, Mech. Mater. 191 (2024) 104952, https://doi.org/10.1016/j.mechmat.2024.104952.
[33] Y. Xu, H. Zhang, E. Schlangen, M. Luković, B. Šavija, Cementitious cellular composites with auxetic behavior, Cem. Concr. Compos. 111 (2020) 103624, https://doi.org/10.1016/j.cemconcomp.2020.103624.
[34] J. Xie, Y. Xu, Z. Wan, A. Ghaderiaram, E. Schlangen, B. Šavija, Auxetic cementitious cellular composite (ACCC) PVDF-based energy harvester, Energy Build. 298 (2023) 113582, https://doi.org/10.1016/j.enbuild.2023.113582.
[35] J. Xie, Y. Xu, Z. Meng, M. Liang, Z. Wan, B. Šavija, Peanut shaped auxetic cementitious cellular composite (ACCC), Constr. Build. Mater. 419 (2024) 135539, https://doi.org/10.1016/j.conbuildmat.2024.135539.
[36] Y. Xu, B. Šavija, 3D auxetic cementitious-polymeric composite structure with compressive strain-hardening behavior, Eng. Struct. 294 (2023) 116734, https://doi.org/10.1016/j.engstruct.2023.116734.
[37] M. Chen, S. Fang, G. Wang, Y. Xuan, D. Gao, M. Zhang, Compressive and flexural behaviour of engineered cementitious composites based auxetic structures: an experimental and numerical study, J. Build. Eng. 86 (2024) 108999, https://doi.org/10.1016/j.jobe.2024.108999.
[38] Y. Xu, Z. Meng, R.J.M. Bol, B. Šavija, Spring-like behavior of cementitious composite enabled by auxetic hyperelastic frame, Int. J. Mech. Sci. 275 (2024) 109364, https://doi.org/10.1016/j.ijmecsci.2024.109364.
[39] Y. Xu, B. Šavija, Auxetic cementitious composites (ACCs) with excellent compressive ductility: experiments and modeling, Mater. Des. 237 (2024) 112572, https://doi.org/10.1016/j.matdes.2023.112572.
[40] V. Nguyen-Van, J. Liu, C. Peng, G. Zhang, H. Nguyen-Xuan, P. Tran, Dynamic responses of bioinspired plastic-reinforced cementitious beams, Cem. Concr. Compos. 133 (2022) 104682, https://doi.org/10.1016/j.cemconcomp.2022.104682.
[41] Y. Xu, E. Schlangen, M. Luković, B. Šavija, Tunable mechanical behavior of auxetic cementitious cellular composites (CCCs): experiments and simulations, Constr. Build. Mater. 266 (2021) 121388, https://doi.org/10.1016/j.conbuildmat.2020.121388.
[42] R. Ouadday, A. Marouene, G. Morada, A. Kaabi, R. Boukhili, A. Vadean, Experimental and numerical investigation on the impact behavior of dual-core composite sandwich panels designed for hydraulic turbine applications, Compos. Struct. 185 (2018) 254–263, https://doi.org/10.1016/j.compstruct.2017.11.007.
[43] X. Zhu, M. Kang, Y. Fei, Q. Zhang, R. Wang, Impact behavior of concrete-filled steel tube with cruciform reinforcing steel under lateral impact load, Eng. Struct. 247 (2021) 113104, https://doi.org/10.1016/j.engstruct.2021.113104.
[44] H. Le Minh, S. Khatir, M. Abdel Wahab, T. Cuong-Le, A concrete damage plasticity model for predicting the effects of compressive high-strength concrete under static and dynamic loads, J. Build. Eng. 44 (2021) 103239, https://doi.org/10.1016/j.jobe.2021.103239.
[45] H. Othman, H. Marzouk, Applicability of damage plasticity constitutive model for ultra-high performance fibre-reinforced concrete under impact loads, Int. J. Impact Eng. 114 (2018) 20–31, https://doi.org/10.1016/j.ijimpeng.2017.12.013.
[46] V. Nguyen-Van, C. Peng, P.J. Hazell, J. Lee, H. Nguyen-Xuan, P. Tran, Performance of meta concrete panels subjected to explosive load: Numerical investigations, Struct. Concr. n/a (2023), https://doi.org/10.1002/suco.202200749.
[47] A. Shishegaran, M.R. Khalili, B. Karami, T. Rabczuk, A. Shishegaran, Computational predictions for estimating the maximum deflection of reinforced concrete panels subjected to the blast load, Int. J. Impact Eng. 139 (2020) 103527, https://doi.org/10.1016/j.ijimpeng.2020.103527.
[48] L.J. Malvar, C.A. Ross, Review of Strain Rate Effects for Concrete in Tension, ACI Materials Journal, 95 10.14359/418.
[49] V. Mechtcherine, O. Millon, M. Butler, K. Thoma, Mechanical behaviour of strain hardening cement-based composites under impact loading, Cem. Concr. Compos. 33 (2011) 1–11, https://doi.org/10.1016/j.cemconcomp.2010.09.018.
[50] M. Nöldgen, O. Millon, K. Thoma, E. Fehling, Hochdynamische materialeigenschaften von ultrahochleistungsbeton (UHPC), Beton- und Stahlbetonbau 104 (2009) 717–727, https://doi.org/10.1002/best.200900038.
[51] A.C.C. Trindade, A.A. Heravi, I. Curosu, M. Liebscher, F. de Andrade Silva, V. Mechtcherine, Tensile behavior of strain-hardening geopolymer composites (SHGC) under impact loading, Cem. Concr. Compos. 113 (2020) 103703, https://doi.org/10.1016/j.cemconcomp.2020.103703.
[52] H. Schuler, C. Mayrhofer, K. Thoma, Spall experiments for the measurement of the tensile strength and fracture energy of concrete at high strain rates, Int. J. Impact Eng. 32 (2006) 1635–1650, https://doi.org/10.1016/j.ijimpeng.2005.01.010.
[53] R.J. Thomas, A.D. Sorensen, Review of strain rate effects for UHPC in tension, Constr. Build. Mater. 153 (2017) 846–856, https://doi.org/10.1016/j.conbuildmat.2017.07.168.
[54] M. Ketabdari, E. Toraldo, M. Crispino, V. Lunkar, Evaluating the interaction between engineered materials and aircraft tyres as arresting systems in landing overrun events, Case Stud. Constr. Mater. 13 (2020) e00446, https://doi.org/10.1016/j.cscm.2020.e00446.
[55] K. Barri, Q. Zhang, J. Kline, W. Lu, J. Luo, Z. Sun, B.E. Taylor, S.G. Sachs, L. Khazanovich, Z.L. Wang, A.H. Alavi, Multifunctional nanogenerator-integrated metamaterial concrete systems for smart civil infrastructure, Adv. Mater. 35 (2023) 2211027, https://doi.org/10.1002/adma.202211027.
[56] J. Lubliner, J. Oliver, S. Oller, E. Oñate, A plastic-damage model for concrete, Int. J. Solids Struct. 25 (1989) 299–326, https://doi.org/10.1016/0020-7683(89)90050-4.
[57] J. Lee, L. Fenves, Gregory, Plastic-Damage Model for Cyclic Loading of Concrete Structures, J. Eng. Mech. 124 (1998) 892–900, https://doi.org/10.1061/(ASCE)0733-9399(1998)124:8(892).
[58] H. Martín-Sanz, B. Herraiz, E. Brühwiler, E. Chatzi, Shear-bending failure modeling of concrete ribbed slabs strengthened with UHPFRC, Eng. Struct. 222 (2020) 110846, https://doi.org/10.1016/j.engstruct.2020.110846.
[59] R. Faria, J. Oliver, M. Cervera, A strain-based plastic viscous-damage model for massive concrete structures, Int. J. Solids Struct. 35 (1998) 1533–1558, https://doi.org/10.1016/S0020-7683(97)00119-4.
[60] J.Y. Wu, J. Li, R. Faria, An energy release rate-based plastic-damage model for concrete, Int. J. Solids Struct. 43 (2006) 583–612, https://doi.org/10.1016/j.ijsolstr.2005.05.038.
[61] D.-C. Feng, X.-D. Ren, J. Li, Softened damage-plasticity model for analysis of cracked reinforced concrete structures, J. Struct. Eng. 144 (2018) 04018044, https://doi.org/10.1061/(ASCE)ST.1943-541X.0002015.
[62] W. Wan, J. Yang, G. Xu, Y. Liu, Determination and evaluation of Holmquist-Johnson-Cook constitutive model parameters for ultra-high-performance concrete with steel fibers, Int. J. Impact Eng. 156 (2021) 103966, https://doi.org/10.1016/j.ijimpeng.2021.103966.
[63] J. Wu, J. Ning, T. Ma, The dynamic response and failure behavior of concrete subjected to new spiral projectile impacts, Eng. Fail. Anal. 79 (2017) 547–564, https://doi.org/10.1016/j.engfailanal.2017.05.037.
[64] Q. Yu, Z. Chen, J. Yang, K. Rong, Numerical study of concrete dynamic splitting based on 3d realistic aggregate mesoscopic model, : Mater. 14 (2021).
[65] S. Xu, P. Wu, C. Wu, Calibration of KCC concrete model for UHPC against low-velocity impact, Int. J. Impact Eng. 144 (2020) 103648, https://doi.org/10.1016/j.ijimpeng.2020.103648.
[66] F. Zhou, H. Wu, Y. Cheng, Perforation studies of concrete panel under high velocity projectile impact based on an improved dynamic constitutive model, Def. Technol. 27 (2023) 64–82, https://doi.org/10.1016/j.dt.2022.09.004.
[67] Z. Wu, J. Zhang, H. Yu, H. Ma, 3D mesoscopic investigation of the specimen aspect-ratio effect on the compressive behavior of coral aggregate concrete, Compos. Part B: Eng. 198 (2020) 108025, https://doi.org/10.1016/j.compositesb.2020.108025.
[68] J. Lai, W. Sun, Dynamic behaviour and visco-elastic damage model of ultra-high performance cementitious composite, Cem. Concr. Res. 39 (2009) 1044–1051, https://doi.org/10.1016/j.cemconres.2009.07.012.
[69] Q. Fu, D. Niu, D. Li, Y. Wang, J. Zhang, D. Huang, Impact characterization and modelling of basalt-polypropylene fibre-reinforced concrete containing mineral admixtures, Cem. Concr. Compos. 93 (2018) 246–259, https://doi.org/10.1016/j.cemconcomp.2018.07.019.
[70] J. Lu, T. Yin, W. Guo, J. Men, J. Ma, Z. Yang, D. Chen, Dynamic response and constitutive model of damaged sandstone after triaxial impact, Eng. Fail. Anal. 163 (2024) 108450, https://doi.org/10.1016/j.engfailanal.2024.108450.
[71] S. Hou, S. Liang, D. Liu, Study on dynamic mechanical properties and constitutive model of granite under constant strain rate loading, Constr. Build. Mater. 363 (2023) 129975, https://doi.org/10.1016/j.conbuildmat.2022.129975.
[72] D. Lai, F. Nocera, C. Demartino, Y. Xiao, P. Gardoni, Probabilistic models of dynamic increase factor (DIF) for reinforced concrete structures: A Bayesian approach, Struct. Saf. 108 (2024) 102430, https://doi.org/10.1016/j.strusafe.2024.102430.
[73] CEB-FIP, CEB-FIP model code 2010: Design code, Thomas Telford Publishing, 2010.

[74] S.D. Adhikary, L.R. Chandra, A. Christian, K.C.G. Ong, SHCC-strengthened RC panels under near-field explosions, Constr. Build. Mater. 183 (2018) 675–692, https://doi.org/10.1016/j.conbuildmat.2018.06.199.
[75] X.-q Li, Q.-j Chen, J.-F. Chen, J.-z Liao, Y. Lu, Dynamic increase factor (DIF) for concrete in compression and tension in FE modelling with a local concrete model, Int. J. Impact Eng. 163 (2022) 104079, https://doi.org/10.1016/j.ijimpeng.2021.104079.
[76] H. Wu, Q. Zhang, F. Huang, Q. Jin, Experimental and numerical investigation on the dynamic tensile strength of concrete, Int. J. Impact Eng. 32 (2005) 605–617, https://doi.org/10.1016/j.ijimpeng.2005.05.008.